manuscript submitted to *JGR: Solid Earth*

Tectonic low-frequency earthquakes in Shikoku, Japan: source scaling, size distribution and observational limits

M. Supino[1], N. M. Shapiro[2,3], J.P. Vilotte[1], N. Poiata[1,4] and K. Obara[5]

[1]Université de Paris, Institut de physique du globe de Paris, CNRS (UMR7154), F-75005 Paris, France.

[2]Institut des Sciences de la Terre, Université Grenoble-Alpes, CNRS (UMR5275), F-38058 Grenoble, France.

[3]Schmidt Institute of Physics of the Earth, Russian Academy of Sciences, Moscow, Russia.

[4]National Institute for Earth Physics, 12 Călugăreni, Măgurele, 077125 Ilfov, Romania.

[5]Earthquake Research Institute, University of Tokyo, Bunkyo, Tokyo 113-0032, Japan.

Corresponding author: Mariano Supino

Key Points:

- Cubic moment-duration scaling and high-frequency source spectra decay are observed for LFEs continuously detected in Shikoku over 3 years.
- The self-similar scaling is stable in time and does not change when low-frequency earthquake bursts occur following slow slip events.
- Noise-related observational limits may taper the size distribution of LFEs at both edges of the usually explored seismic moment domain.

Abstract

Low-frequency earthquakes are peculiar energy-release events mostly occurring at the transition between the seismogenic and the freely creeping zones of a subducting slab. The source characterization of these events is of fundamental importance to understand physical processes that govern the slow out of equilibrium evolution of the subduction interface that may lead to the generation of large, destructive earthquakes. Nevertheless, their source mechanisms still remain unclear. Here, we estimate the source parameters of ~23,000 low-frequency earthquakes continuously detected from 2013 to 2015 in Shikoku, Japan. We show that a cubic moment-duration scaling characterizes these events, suggesting a self-similar process as for regular earthquakes. However, their high-frequency fall-off suggests an omega-cube decay in contrast to the omega-squared model of earthquakes. Source characteristics do not change when low-frequency earthquake bursts occur during the analyzed three years. On the other hand, we observe a coherent along-strike variation of the product of stress drop and the cube of rupture velocity, possibly related to a weaker behavior of tremor patches in central Shikoku. Secondary microseismic noise and network-dependent completeness magnitude lead to missing event detections that do not allow discriminating between Gutenberg-Richter event size distribution and any deviation from it. Our findings suggest that the same observational limits might affect world-wide detection of low-frequency earthquakes.

1 Introduction

Low frequency seismicity (tremors and earthquakes) has been known for long time in volcanology (e.g., Chouet, 1996) and evidenced more recently in association with tectonic fault zones (e.g., Frank et al., 2013, 2014; Nadeau & Dolenc, 2005; Obara, 2002; Payero et al., 2008; Rogers & Dragert, 2003; Shelly et al., 2006, 2007). Low frequency seismicity is characterized by signals with rather weak amplitudes and depleted in high frequencies when comparing with regular earthquakes (Abercrombie, 2015) releasing similar energy (a few Hz instead of a few tens of Hz). One of possible explanations for this difference in frequency content is different physical process responsible for generation of regular earthquakes and of low frequency seismicity. So far, this point of view is dominant in volcano-seismology: the so called “volcano-tectonic” earthquakes are believed to originate from faulting (similar to regular tectonic earthquakes) while the origin of low-frequency seismicity is most often attributed to fluid-enhanced processes within magmatic or hydrothermal systems.

Following the initial discovery of the low-frequency tectonic tremors in Japan and in analogy with volcanic tremors, their generation by fluids released from dehydration of the subducted slab has been considered as one of possible scenarios (Kao et al., 2005; Katsumata & Kamaya, 2003; Obara, 2002). Later studies (Shelly et al., 2006) showed that tectonic tremors are strongly associated with low-frequency earthquakes (LFE), and even suggested that tremors could be a swarm of many LFEs (Shelly et al., 2007). It is worth to mention that similar association between tremors and LFE was also previously suggested in volcano seismology (Fehler, 1983). The location of the LFE sources in the close vicinity of the subduction interface and their radiation patterns suggested that they are likely generated by shear faulting along the plate interface (Ide, Shelly, et al., 2007; Shelly et al., 2007). Finally, a close association of LFEs and tremors with geodetically observed slow-slip events (SSE) has been reported (Hirose et al., 1999; Obara & Hirose, 2006; Rogers & Dragert, 2003). Very low-frequency earthquakes (VLFs) (Ghosh et al., 2015; Ito et al., 2007; Obara & Ito, 2005) complete the broad class of slow earthquake phenomena. Numerous observations showed a collective activity of the different slow earthquake phenomena suggesting they are sparse

observations probing the collective dynamics of a particular mode of shear failure at the transition zone between locked and continuously creeping segments of the fault (Ide, 2014; Obara & Kato, 2016).

One of the main reasons for the interest in the slow earthquakes phenomena is that new seismological and geodetic observations can provide us with information about the slow transient energy-release processes occurring during the evolution of active fault zones in between large tectonic earthquakes, which eventually play a fundamental role in their occurrence (Obara & Kato, 2016). A correct interpretation of these observations requires physics-based understanding of the driving processes. Today, a classical hypothesis is that a-seismic deformation and low-frequency seismic radiation are both signatures of fault-slip events on regions of the fault interface where high pore fluid pressure plays an important role (e.g. Audet et al., 2009). A fluid-rich and over-pressurized shear zone can be prone to mechanical conditions responsible to "slow" transient deformation and slip (e.g., Behr & Bürgmann, 2020). It has also been suggested that a rapid fluid pressure migration and diffusion may control the spatial-temporal patterns of the slow earthquake activity (e.g., Bernaudin & Gueydan, 2018; Cruz-Atienza et al., 2018; W. B. Frank et al., 2015) and even possibly radiate seismic energy (Shapiro et al., 2018).

Empirical scaling laws between earthquake source parameters such as seismic moment, size, duration, and energy (Aki, 1967; Kanamori & Anderson, 1975), and magnitude-dependent earthquake recurrence statistics (Gutenberg & Richter, 1944; Rundle, 1993) are among key elements for understanding the physics of regular earthquakes source in the framework of scale-invariant rupture model. The universality of these relations has been verified with numerous datasets representing natural tectonic and laboratory earthquakes over a very broad range of magnitudes. Observed deviation from these celebrated "tectonic earthquake" relations could be the manifestation of different source mechanism, in particular of the importance of fluids (e.g., Harrington & Benson, 2011).

Further understanding of the physics of the sources of slow earthquake phenomena requires a careful analysis of scaling and statistical laws between the different parameters that can be measured from their observed signals (similar to regular earthquakes). To date, important questions that still remain to be answered are: do universal scaling laws exist for an ensemble of slow earthquake phenomena or are these scaling relations different for different slow earthquake phenomena; do these laws vary geographically depending on tectonic and fluids environment? Studying these scaling laws will eventually help us to understand if there is a single source mechanism for the broad class of slow earthquake phenomena or different mechanisms, stress-drops, etc.

In their pioneering study, Ide et al. (2007), combining different seismological and geodetic observations of slow earthquakes reported by different authors, suggested a linear scaling between seismic moment M_0 and source duration T across different scales, in contrast to the cubic moment-duration scaling ($M_0 \propto T^3$) observed for regular earthquakes (Aki, 1967; Allmann & Shearer, 2009). This relation has been revised with more available observation by Gomberg et al. (2016) who proposed a transition between a cubic and a linear scaling due to a scale-bounded process for the longest durations events. Combing different types of observations and processing from different studies can be problematic because of the strong inhomogeneity of the resulting catalogs. As such, studies focusing on scaling properties of one particular type of slow earthquakes observations and processing can be more robust. Several studies where a single component of the slow earthquake phenomena has been considered have been reported in recent literature.

Bostock et al. (2015) reported an almost constant source duration for LFEs occurring along the Cascadia subduction zone ($M_0 \propto f_c^{-10}$, f_c corner frequency $\propto T^{-1}$). A similar scaling has been found for LFEs in Guerrero, Mexico by Farge et al. (2020). A very different result has been obtained by Supino et al. (2020) who showed a regular earthquake like moment-duration scaling measuring corner frequency and seismic moment for LFEs detected in Nankai ($M_0 \propto f_c^{-3}$). Similar regular scaling ($M_0 \propto T^3$) is reported by Michel et al. (2019) for slow slip events (SSE) in the Cascadia megathrust, and by Frank and Brodsky (2019) for SSEs along the Mexican subduction zone. However, the SSE durations reported in these two studies differ by several orders of magnitudes.

A different type of scaling relation has been investigated for tectonic tremors (Maury et al., 2018) and VLFs (Ide, 2016; Ide & Yabe, 2014; Maury et al., 2016). These studies reported a linear relation between the radiated seismic energy and seismic moment, which is similar to regular earthquake scaling, however, with measured energies being few orders of magnitude smaller.

Event size distribution of slow earthquakes is even more controversial: in recent years different results have been reported, varying from Gutenberg-Richter distributions (G-R) with b-value close to what is largely observed for regular earthquakes ($b \approx 1$) or larger b-values ($b > 2$), to non-G-R distributions: Tapered Gutenberg-Richter (TGR) distribution (Kagan, 2002), related to a scale-bounded source process for larger events, or exponential distribution, associated with a complete scale-limited process. In northern Cascadia, Kao et al. (2010) observed a b-value = 1 for tremor bursts, selecting a narrow moment magnitude domain (M_w = 1.0 – 1.7). In the same region, Wech et al. (2010) reported the same b-value for major episodic tremor and slip events (ETS) and inter-ETS tremor swarms, assuming $M_0 \propto T$. Sweet et al. (2014) analyzing LFEs occurring at the down-dip edge of the region, found b = 4.2 when larger events were selected. They suggested that an exponential distribution would better describe the observations in a larger domain. Bostock et al. (2015) found b-values ranging from 6.3 to 7.5 for LFEs in southern Vancouver Island, again when selecting larger events. Finally, Chestler and Creager (2017) suggested an exponential distribution for LFEs beneath the Olympic Peninsula. In Japan, Ito et al. (2009) studying VLFs in the southwestern region, along the Nankai subduction zone, concluded that it is not possible to discriminate between G-R or exponential distribution in the observed narrow moment magnitude domain (M_w = 3.0 – 3.8). For semi-volcanic LFEs beneath Osaka Bay, Aso et al. (2011) reported a b-value = 2. Subsequently, Aso et al. (2013) extended the analysis to tectonic and volcanic LFEs, suggesting non-G-R distribution for the first class of events, and G-R for the second. For VLFs in the Ryukyu Trench, Nakamura and Sunagawa (2015) reported b-values = 2.63 – 3.74. Exponential distribution was suggested for tremor bursts in central and southwestern Japan (Hiramatsu et al., 2008; Watanabe et al., 2007; Yabe & Ide, 2014). Nakano et al. (2019) proposed a TGR distribution for shallow, tectonic tremor in the Nankai Trough.

In summary, the studies of the slow earthquake scaling relations reported to date do not provide a simple support for a universal behavior and a simple or unique source process. This ensemble of results can be considered as arguments in favor of a diversity of physical/fluids conditions and mechanisms acting in the slow earthquake source regions. At the same time, many of the reported results can have significant limitations related to possible heterogeneous and imbalanced catalogs that were used, and associated with the different assumptions used for the detection and selection of the analyzed seismic and geodetic events. It is worth to mention that establishing universal scaling laws for regular earthquakes required numerous studies over several decades. Analyzing slow earthquake phenomena is in a sense a more difficult task because of the very low signal-to-noise ratio of most of the associated observations. As a result, the detection and classification of

the related signals is highly uncertain and compilation of homogenous, well-balanced and representative catalogs is challenging. A simple example is the difficulty to define tectonic tremor events whose onset detection depends on ad-hoc a-priori parameters. A similar issue has been recently pointed out for SSEs by Frank (2016) and Frank et al. (2018) who suggested that slow slip occurs over a wide spectrum of time scales and that large SSEs can be composed of many smaller size events with a scale-invariant distribution of durations implying that geodetic measurements of SSE durations can be largely overestimated because of their lack of temporal resolution. Another difficulty is that catalogs of particular slow earthquake events cover rather small range of magnitudes (comparing to catalogs of regular earthquakes). As a result, inferences from the obtained parameters distributions require a very careful statistical analysis and, in particular, should be checked for possible biases related to detection limits and incomplete catalogs.

In this study, we focus on tectonic LFEs. They are detected as impulsive signals with deterministic (S-wave) moveouts over a network of receivers and characterized by dominant frequencies in the 1 – 10 Hz band implying well localized in time and space sources (Brown et al., 2009; Katsumata & Kamaya, 2003; Shelly et al., 2006). As such, definition of a single LFE is less ambiguous comparing to the definitions of a single SSE or a single tremor event. At the same time, because of the low signal-to-noise ratio, LFE detections remain difficult and highly uncertain, implying that their significance should be interpreted in probabilistic terms. With these considerations, the goal of our study is to perform a statistical analysis of a large and homogeneous LFE catalog. By homogeneity of the catalog we imply that it is built by systematically applying a well-defined method with a minimum number of clearly defined and described a-priory assumptions. Most of LFEs observed so far occur during longer lasting, continuous episodes of tectonic tremors (Obara & Hirose, 2006; Shelly et al., 2007). As such, some of the existing LFE catalogs are limited to periods of tremor activity, which is a strong a-priori and possibly limiting assumption when considering in particular the difficulty to precisely define periods of tremor activity. Therefore, we prefer here to analyze a catalog that is directly built from an analysis of a several years of continuous seismic records.

We use four years of data form Shikoku, Japan – one of the regions where slow earthquake activity is best characterized and covered by a large and dense seismic network. We apply a well-documented method (Poiata et al., 2016, 2018) for detection of potential LFE. This technique seeks to minimize as possible the a-priori information on the frequency content of the signals, and do not assume any template event. We then analyze the displacement spectra of the detected events by applying a probabilistic method (Supino et al., 2019) for earthquake source characterization. We use the two quality selection criteria of this method to exclude noisy or possible false detections from our analysis, keeping only the most robust information from the catalog. First, we extract the frequency band in which the spectral signal-to-noise ratio is larger than 1.25. Detections with an empty or extremely narrow frequency band are rejected, as they are most likely associated with stationary signals rather than short-duration impulsive transients. This is our main selection step, and ~90% of rejections are due to this criterion. We then invert the spectra (Supino et al., 2019, 2020), assuming a generalized Brune's spectral model (Brune, 1970), of the remaining detections in the selected frequency band, estimating the joint probability density function (PDF) of the seismic moment, corner frequency, and high frequency decay exponent. At this stage, we apply the second quality criterion rejecting all the detections which exhibit at least one unconstrained source parameter PDF (~10% of total rejections). Possible reasons might be a strong misfit between the observed data and the data predicted by the assumed spectral model (forward

operator), or a too narrow frequency band available for the inversion (low-dimensional data space). The two quality selection criteria leave us with ~17% of the initial automatic LFE catalog. We use the source parameters inferred from the selected detections to investigate LFEs source characteristics, analyzing the variation in time and space of those parameters and derived scaling coefficients such as the moment-duration scaling parameter. In addition, the time analysis allows us to identify and exclude contaminations from aftershock sequences of strong tectonic earthquakes. Finally, we exploit the fully automated and probabilistic approach on which this study relies to analyze the event size distribution of LFEs, together with possibly related observational limits.

2 Automatic LFE catalog from continuous data

We perform an automatic detection and location of LFEs in Shikoku, Japan, analyzing the continuous velocity seismograms recorded during the time-period of January 2013 – December 2016, at 33 stations of the high-sensitivity seismic network (Hi-net) run by the National Research Institute for Earth Science and Disaster Resilience (NIED) (Okada et al., 2004). The selected 33 stations cover the area of the Shikoku region that is characterized by the highest ratio of tremor energy release along the Nankai through (Annoura et al., 2016) and as such that is also expected to have a high rate of LFE activity.

We use the automatic network-based detection and location scheme BackTrackBB (Poiata et al., 2016, 2018), which exploits frequency-selective coherence of statistical features across the network stations to extract the onset of short-duration, impulsive transients within the continuous recorded seismic signals and to locate their sources in space and time. This well documented scheme was demonstrated to be efficient for extracting narrow-band, small-magnitude events from noisy records such as those corresponding to LFEs buried in tectonic tremor signals without requiring previously detected template events (Poiata et al., 2018). The workflow consists of two main parts: a signal processing and a detection and location analysis part. The signal processing part builds time-series of characteristic functions (CFs) extracting targeted properties of the continuous non-stationary signals. It makes use of a signal time-frequency analysis to extract relevant frequency-dependent information, and account for potential multi-scale signal's characteristics. In the detection-location analysis part, station-pair time-delay estimate (TFE) functions are built from local time correlation of the CFs time-series and then projected and summed onto a 3D spatial grid assuming a given seismic phase and a seismic velocity model. This step provides spatial likelihood maps of the source being located at a given position of the 3D grid. The event's location is extracted as the maximum likelihood, together with location uncertainties. In this study, the detection and location of LFE sources is performed using a frequency-dependent kurtosis CF. The kurtosis CF is calculated from the combined horizontal components — recorded at the selected Hi-net stations — filtered with a multi-band filter bank of 20 logarithmically spaced filters spanning the frequency range of 2.0 – 15.0 Hz, that corresponds to the predominant frequency range in which most of the LFEs radiated energy is observed (Obara & Hirose, 2006). The 3-D grid used in the location scheme covers the targeted region of Shikoku (centered at 33.575 °N and 132.850 °E) with an (X, Y, Z) extension of 292 km × 190 km × 100 km (Figure 1) and a 1 km^3 element grid-size. The predominant phase on the horizontal component of the recorded LFE signal is assumed to be the S-wave phase (Obara, 2002; Shelly et al., 2006). Theoretical S-wave travel times, associated to the 3-D grid, were estimated using the Grid2Time routine of NonLinLoc (Lomax, 2005, 2008), and the 1-D velocity model of Kubo et al. (2002).

Station selection plays an important role in the detection and source location of small-amplitude signals generated by low-magnitude LFEs, often buried into complex tectonic tremor signal during periods of intense tectonic tremor sequences. As such, a preliminary step was implemented in the analysis, which corresponds to the detection and location of tectonic tremor sources using an energy envelope characteristic function. Locations of tectonic tremor sources —averaged over one hour of activity — are estimated following a clustering scheme similar to Obara et al. (2010), and used to select the distribution of stations for the detection and location of LFEs. This procedure closely follows the analysis in Poiata et al. (2018) and is based on the assumption that LFEs and tectonic tremor are different signatures of the same process, and thus have coincident source occurrence in space and time. At the same time, the signature of tectonic tremor on energy envelopes is more easily observable over the larger distances.

The final raw LFE catalog built from the automatic detection-location method consists of more than 134000 events, which may include earthquakes and false detections. In the source characterization analysis, applying the quality selection criteria described in section 3.1, ~17% of the events in this catalog (Figure S1) are retained leading to the estimation of the source parameters of ~23,000 LFEs (Figure 1). Also, in section 4.2.1 we show that the aftershocks of two large earthquakes ($M > 6.5$), which occurred during the year 2016 close to Shikoku region, might be the cause of a significant number of false detections contaminating the raw catalog. We have therefore chosen to exclude this year from our analysis.

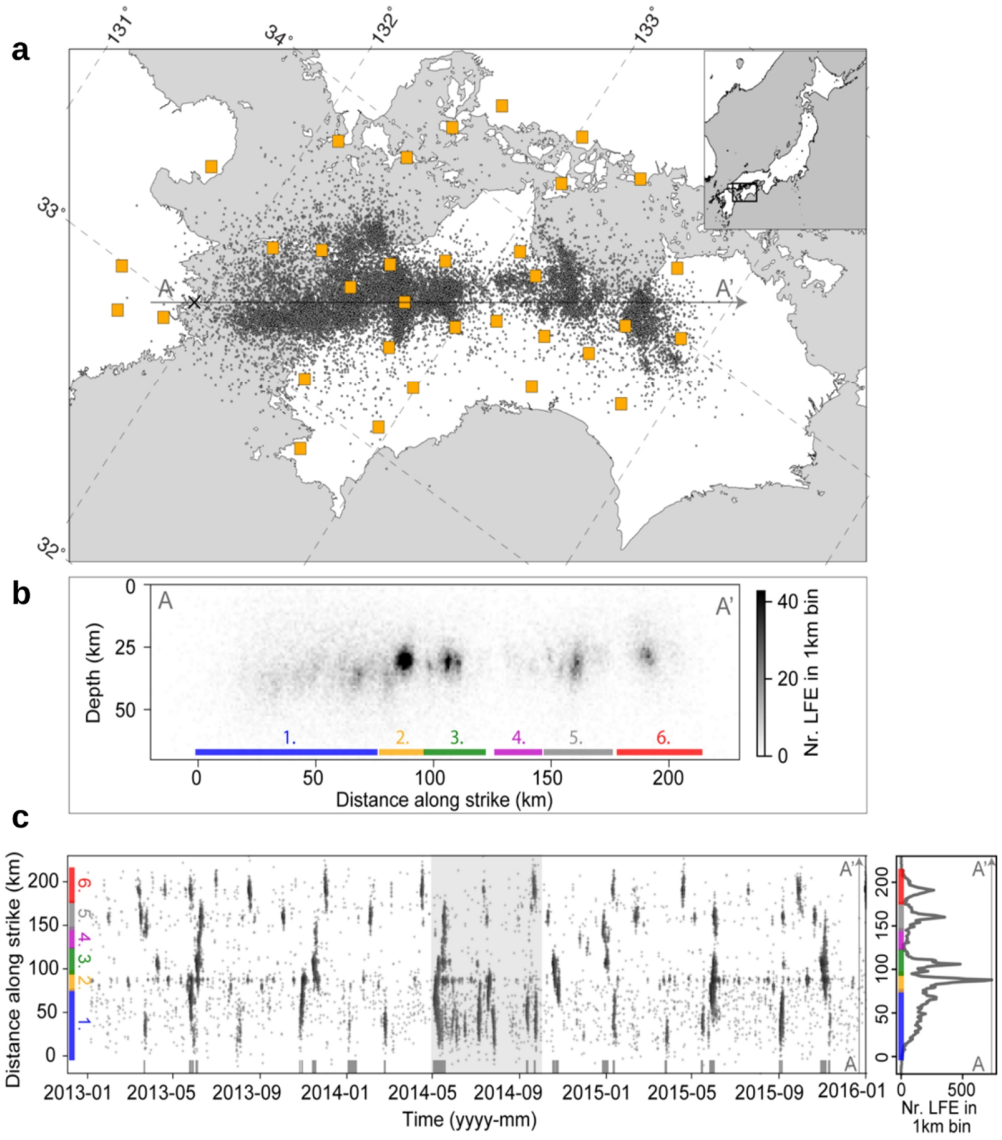

Figure 1. Overview of the study area and distribution of analyzed LFE. **a,** Map view of the Shikoku region. Grey circles indicate locations of the analyzed LFEs and orange squares show the Hi-net stations used in the study. Thin grey arrow (A-A') indicates the direction of N 40º E, along the strike of the subducting slab that defines the projection direction. Black cross indicates the zero reference point at 33.00º N and 131.95º E. The upper right inset shows the geographic location of Shikoku region. **b,** Depth cross-section of the analyzed LFEs projected along strike direction (A-A') shown as number of events per 1km^2 bin. Colored horizontal lines, and the numbers above, outline the LFE source regions defined based on the statistical characteristics of LFE activity over 3-year period. **c,** Space-time plot of LFE sources for the analyzed 3-year time period. Events are projected along the strike direction A-A' defined in panel (a). Colored vertical bars and the numbers correspond to the defined LFE source regions. Grey shaded rectangle indicates timing of long-term slow-slip event (SSE) in Bungo Channel (Ozawa, 2017). Grey horizontal bars correspond to the short-term SSEs occurring in Shikoku region, reported by AIST and NIED.

2.1 JMA LFE catalog

In addition, we analyze ~3,000 LFEs extracted from the unified earthquake catalog provided by the Japanese Meteorological Agency (JMA) (Kano, Aso, et al., 2018; Katsumata & Kamaya, 2003) in the same region and time period explored by the automatic detection and location method (Figure S2a). In contrast, JMA events have been located using manually picked arrival times of P- and S-waves. As such, source parameters inferred from this manual catalog represent an important benchmark for our results. The probability of observing false detections in this catalog is expected to be quite small, while the probability of missing detections is undoubtedly larger than in our automatic catalog.

3 Estimation of source parameters

We use the probabilistic method of Supino et at. (2019) to evaluate the joint PDF of the source parameters: seismic moment (M_0), corner frequency (f_C) and high-frequency source spectra decay exponent (γ) of a generalized Brune's spectral model $\tilde{S}(f)$ (Brune, 1970):

$$\tilde{S}(M_0, f_C, \gamma; f) = M_0/(1 + (f/f_C)^\gamma) \quad (1)$$

The observation we invert is the S-wave far-field displacement amplitude spectrum $\tilde{u}(f)$, which can be modeled as the product between the source spectrum $\tilde{S}(f)$ and the Green's propagator spectrum $\tilde{G}(f)$. We assume an anelastic attenuation independent of the frequency for $\tilde{G}(f)$, and assess the effects of this assumption on the source parameters estimations by testing different attenuation models (see section 5.1.1). The forward operator is thus defined as a mapping from the 3-D model space spanned by the three source parameters of eq. (1) into the data space defined by the far-field amplitude spectra.

For each parameter, the single-station solution and related uncertainty are respectively the mean and the standard deviation of the corresponding marginal PDF, obtained by integrating the joint PDF (Figure S3). Final event solution is given by the weighted average of single-station solutions, where the weight corresponds to the inverse of the estimated variance. The estimation of the joint PDF allows obtaining source parameter solutions that account for between-parameter correlation (Figure S3d). Moreover, the accurate estimation of the error associated with each single-station observation (Figure S3e), used to infer final event solution (Figure S3c), allows to deal with large uncertainty associated to the narrow frequency band available for the inversion, and with source parameters' variability across different stations for the same event. Addressing all these elements is of fundamental importance for estimating reliable source parameters, particularly when dealing with extremely LFE weak signals.

It is worth noting that in this study the main assumption for the source parameters estimation is coming from the Brune's spectral model on which our forward operator relies, more than from the specific Brune's source model itself. At low frequencies, the source appears as a point, and the spectrum is flat and proportional to the seismic moment M_0. At high frequencies, interference among the radiation emitted from different zones of the source emerges as a spectrum-decay. The crossover region between the two spectral behaviors is thus associated to a corner frequency f_C that is a proxy to the source dimension. Similar spectral shape is derived for different, more physically consistent, source models (Boatwright, 1980; Kaneko & Shearer, 2014; Madariaga, 1976; Sato & Hirasawa, 1973), the main difference being the specific value of the coefficient linking corner frequency to the rupture dimension (see Abercrombie (2021) for a review on the spectral modelling and inversion).

3.1 Quality selection criteria

We use the same forward operator, processing parameters and quality selection criteria described in Supino et al. (2020), which we recall here.

We start from the raw signal, selecting a 4 s S-wave time window around the theoretical arrival times T_S computed using the velocity model of Kubo et al. (2002): $T_S - 1$ s, $T_S + 3$ s. A noise window of the same length is selected before the origin time. The S-wave displacement amplitude spectrum is the observation that we invert to estimate the source parameters, while the noise spectrum is used to define the frequency bandwidth available for the inversion. Specifically, we select the frequency sub-domain in which the S-wave spectrum is at least 1.25-fold the noise (black vertical bars in Figure S3b). This allows inverting the most robust information from the S-wave spectrum, automatically excluding the lowest and highest frequency sub-domains where the information carried by the S-wave and by the noise is practically the same.

To deal with extremely noisy S-wave records or potential false detections, we reject all the spectra that correspond to a selected frequency-band with less than 10 points (Figure S4). This is our main selection step, and ~90% of the event rejections are due to this criterion (Figure S1b). The defined threshold for the minimum required number of points is playing a minor role, since for ~85% of the rejected spectra the selected frequency band is an empty set, meaning that the S-wave and the noise spectra are almost the same in the entire band.

Moreover, we observe spectra for which the low signal-to-noise ratio leads to at least one unconstrained marginal PDF solution (Figure S5). We automatically reject also those records, evaluating the degree of similarity of the marginal PDF with a normal distribution (Supino et al., 2019). Rejections vary from moderately unconstrained solutions, corresponding to a too narrow frequency band available for the inversion (Figure S5a-c), to strongly unconstrained solutions, caused by a large misfit between observed data and model predictions (Figure S5d-f). This criterion also allows rejecting regular earthquakes that contaminate the automatic catalog (Figure S6). However, as we discuss in section 5.2.1, in the case of a strong contamination due to aftershocks of large earthquakes (M > 6.5) occurring at near-regional distances (a few hundred kilometers), regular earthquakes may pass the selection. Overall, PDF-based rejections represent ~10% of total rejections (Figure S1b).

With the quality selection criteria described above, we retain about 17% of the events in the raw catalog derived from the automatic detection-location method (Figure S1). On average, the main effect of this selection is the rejection of events close to the boundaries of the distribution of stations used for detection (Figure S1a).

4. Estimation of scaling coefficients

We estimate the scaling between seismic moment M_0 and corner frequency f_C from a linear regression, according to eq. (2):

$$\log f_C = 1/A' \cdot \log M_0 + B, \tag{2}$$

where log is the common (base 10) logarithm and $A' \equiv 1/A$ is the scaling parameter, that we define as the inverse of the slope coefficient A. Since the corner frequency f_C is inversely proportional to the source duration T (Savage, 1972), the parameter A' equivalently describe the scaling of the seismic moment with duration, $M_0 \propto T^{-A'}$. A scaling parameter $A' = -3$ implies earthquake self-similarity, where stress drop is independent of the earthquake size (moment) (Aki, 1967; Kanamori & Anderson, 1975), when a constant rupture velocity is assumed (Kanamori & Rivera, 2004).

The intercept coefficient B in eq. (2) contains information about the mechanical properties of the subduction interface. Indeed, when A' is fixed to -3, the intercept B can be written as:

$$B = 1/3 \cdot \log(\Delta\sigma \cdot (\beta \cdot k)^3 \cdot C^{-1}) \quad (3)$$

where $\Delta\sigma$ is the static stress drop:

$$\Delta\sigma = C \cdot M_0/r^3, \quad (4)$$

β is the shear-wave velocity in the vicinity of the source and k is the coefficient linking the corner frequency to the source radius r:

$$f_C = k \cdot \beta/r \quad (5)$$

Eq. (4) has been obtained for an elliptical crack in an homogeneous elastic medium (Eshelby, 1957), where r is a characteristic length associated with the source narrowest dimension and C is a factor that depends on the source aspect ratio and the Poisson's ratio (for circular rupture and Poissonian solid, C = 7/16). Eq. (5) is a general relation valid for different source models ranging from an explosion to a shear dislocation (Hanks & Wyss, 1972), and the k coefficient depends on the assumed dynamic or kinematic source rupture model. However, for a given rupture geometry and source rupture model, k only varies with the effective rupture speed v_R and is larger for faster rupture speeds (Kaneko & Shearer, 2014, 2015; Madariaga, 1976; Sato & Hirasawa, 1973; Supino et al., 2020). Therefore, for a specific source model (and fixed Poisson's ratio), the coefficient B of eq. (3) only depends on the stress drop and the effective rupture velocity. The existing trade-off between $\Delta\sigma$ and v_R (Causse & Song, 2015; Chounet et al., 2018; Supino et al., 2020) does not allow to simply constrain their values from the estimation of the intercept B. However, these two quantities are expected to coherently vary with the interface strength. Thus, variation of B can be related to a change of the interface strength due to mechanical and environmental (e.g., fluids) properties of the fault zone and/or to pre-stress conditions.

5. Results

5.1 Average LFE source and scaling parameters in the Shikoku region

Seismic moment, corner frequency and high frequency source decay exponent estimated for ~23,000 LFEs of our automatic catalog (Figure 1) are shown in Figure 2. A scaling between seismic moment and corner frequency emerges over 2 decades of seismic moment (Figure 2a), while the distribution of the high frequency decay exponents is well-constrained around the median value 3.0, with 75% of the solutions between 2.0 and 4.0 (Figure 2b).

We estimate a scaling parameter A' = -3.5 ± 0.8 (see previous section). These are mean and standard deviation of the scaling parameter PDF, that is evaluated with a bootstrap method (Supino et al., 2020) which relies on 300,000 random extractions (Figure S7a). The bootstrap is built starting from bin-averaged corner frequencies and related weighted standard deviations (red circles and vertical bars in Figure 2a), evaluated in narrow intervals (bin-size = 0.08 log M_0) of the explored seismic moment domain. The bin-size is fixed to reduce the effects that unbalanced regions in the seismic moment domain might have on the regression. These estimates represent robust averaged information that takes advantage of the large number of observations in each bin, varying from 125 to 1800 events per bin. Also, they minimize the impact of potential site effects as observations from many stations are averaged.

In each bin, a corner frequency f_C is randomly extracted from the normal distribution defined by the mean and standard deviation of the bin-averaged estimates, and the associated seismic moment M_0 is estimated as the center of the bin. A linear regression is performed according to eq. (2) for estimating the scaling parameter A'. The final PDF of A' is the collection of the 300,000 estimates obtained by repeating the random extractions and subsequent linear regressions. The scaling

parameter uncertainty, evaluated as the standard deviation of the PDF, accounts for the corner frequency variability observed in each bin (vertical bars in Figure 2a).
The observed scaling parameter is consistent with the classical value -3 that characterizes the scaling of regular earthquakes. This result suggests that the LFE rupture size scales with the seismic moment so that, assuming a constant effective rupture velocity as typically done for regular earthquakes, the static stress drop is roughly constant and scale-independent (see eq. (2-5)). It should be noted that the inferred mean value of the scaling parameter slightly differs from -3. This difference could be related to a truncation effect that we observe for corner frequencies lower than 1 Hz, as we discuss in section 5.3.3 (see also Figure S10); the PDF estimated excluding these truncated distributions has a mode of -3.0 (Figure S7b). Otherwise, the difference could indicate that the stress drop moderately scales with the seismic moment (Kanamori & Rivera, 2004), varying within one order of magnitude. The uncertainty associated with our estimation of the scaling parameter, which is directly related to the observed variability of the corner frequency, does not allow to constrain the stress drop at such a resolution and to discriminate between the two models. However, even for regular earthquakes — which in principle should provide much better constrained observations than the weak LFE signals — larger variability is usually observed with stress drops spanning several orders of magnitude (Cocco et al., 2016; Cotton et al., 2013; Oth, 2013).

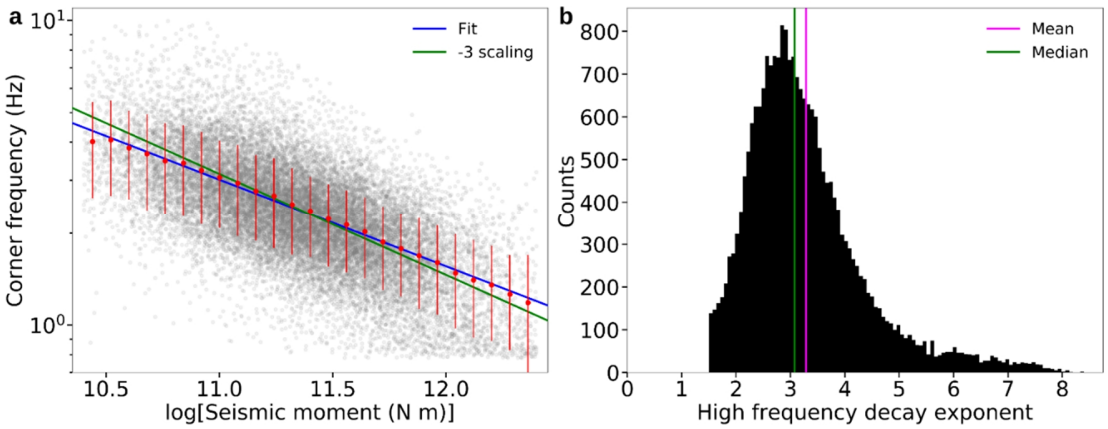

Figure 2. Source parameters of LFEs. **a,** Estimated corner frequency and seismic moment of each LFE source are shown (grey circles), together with bin-averaged (bin-size = 0.08 log M_0) estimates (red circles) and associated weighted standard deviations (red bars). The blue line is the linear regression of the red circles, with a best-fit scaling parameter A' = -3.5, according to eq. (2). The cubic scaling (green line) widely observed for regular earthquakes is very likely (see also Figure S7). **b,** Histogram of the estimated high frequency decay exponents for the LFE sources. The green and magenta vertical bars represent the median and mean of the distribution, respectively. An omega-cubed model (γ = 3) is much more likely than the omega-squared model of regular earthquakes.

Estimation of the LFEs source parameters for the JMA catalog (Figure S2) leads to a similar M_0 – f_C scaling (Figure S2b), with a scaling parameter A' = -3.2 ± 0.5, and to 72% of the high frequency source decay exponents between 2.0 and 4.0 (Figure S2c).

5.1.1 Attenuation effects

We use a theoretical Green's function to model the wave propagation from source to receiver (Supino et al., 2019), assuming a frequency independent quality factor Q = 300, as provided by previous studies (Kubo et al., 2002). To assess possible bias introduced by this assumption, we invert the entire dataset using different attenuation models (Figure S8): a stronger and a weaker frequency-independent attenuation, Q = 100 and Q = 500; the frequency-dependent attenuation, $Q_1(f) = 300\, f^{0.5}$, estimated by Takahashi et al. (2014) for the study area; a stronger attenuation and frequency-dependence, $Q_2(f) = 100\, f^{0.8}$. The different scaling parameters are consistent within 1-σ with those obtained with Q = 300. The largest variation comes from the model Q_2 which leads to a scaling parameter A' = -4.0 ± 0.8 while the median values for the high-frequency decay exponent of the source spectra remain close to the value γ = 3 observed for Q = 300 (Figure S8b). Overall, the source parameter estimates seem to be weakly affected by the different anelastic attenuation models. This could have been expected given the narrow frequency band investigated (~[1 – 10] Hz). Nevertheless, the distribution of the root mean squared errors (RMSEs) show that the choice Q = 300 leads to the minimum averaged RMSE among the explored attenuation models (Figure S8c).

Empirical Green's functions (EGFs) would be the most reliable approach to fully rule out the propagation effects from the observed spectra. However, this technique cannot be systematically applied for the peculiar events analyzed in this study. A good EGF should be co-located with the main event within one source dimension (Abercrombie, 2015). For the weak LFE signals in this study such a resolution cannot be achieved in most of the cases since the uncertainty of the source location is of the order of 10 km (Poiata et al., 2018) and the source dimension of the order of ~[100 – 400] m (Supino et al., 2020). Moreover, selecting the frequency sub-domain where the EGF spectrum is flat and well below its corner frequency may be very difficult, given the range of corner frequencies (~[1 – 9] Hz) and the available bandwidth (~[0.7 – 10] Hz). In addition, a simple use of the spectral ratio in the whole frequency domain would introduce a complexity in the spectral shape that could probably not be resolved within this frequency bandwidth (Supino et al., 2019). Finally, the necessary magnitude difference for the use of EGFs also represents a severe issue, since the moment magnitudes of the entire dataset vary from 0.86 to 2.20. For these reasons, we preferred to use a theoretical Green's function for assessing the effects of the assumed Q factor. The station-averaged procedure that we used cannot account for possible strong, highly localized, attenuation – acting as a low-pass filter close to the LFE source region – which has been proposed as a possible origin for the observed low-frequency content of the LFE signals, by Bostock et al. (2017). However, this would be hard to reconcile with the observed scaling between seismic moment and corner frequency in this study (Figure 2), since in that case an almost constant corner frequency (related to the cutoff frequency of the anelastic attenuation) should appear.

5.2 Variation of source parameters and scaling coefficients in time and space

The activity of the analyzed LFEs is non stationary during the three-year period explored by the ensemble of events considered in Figure 2, and can change significantly at small time scales (weeks to months), for example in relation with the occurrence of short-term and long-term SSEs (Maeda & Obara, 2009; Poiata et al., 2018). To assess the robustness of our results, we analyze the temporal variation of the source parameters by estimating the moment-duration scaling parameter A' and the median value of the high-frequency decay exponent ($\tilde{\gamma}$) of the source spectra for all events occurring in a 2-month moving time window, with a 15-day time-shift (Figure 3). Both parameters A' and $\tilde{\gamma}$ fluctuate around the estimates obtained for the entire catalog, without any significant deviation. As such, correlation with the variation in time of LFEs (grey dotted line in Figure 3) or

SSEs (grey and red horizontal bars in Figure 3) activity seems very unlikely. A similar result is also obtained when analyzing LFEs detected by JMA (Figure S2d). Differently from the previous analysis, here we do not compute bin-averaged corner frequencies because of the limited number of events in each selected time window (or in the along-strike region). The scaling parameter *A'* is simply estimated from a linear regression using all events in the time window, according to eq. (2). We remind that events detected during 2016 are not considered in this study because the catalog is contaminated by spurious detection associated to the aftershocks of two strong earthquakes (as discussed in the following subsection).

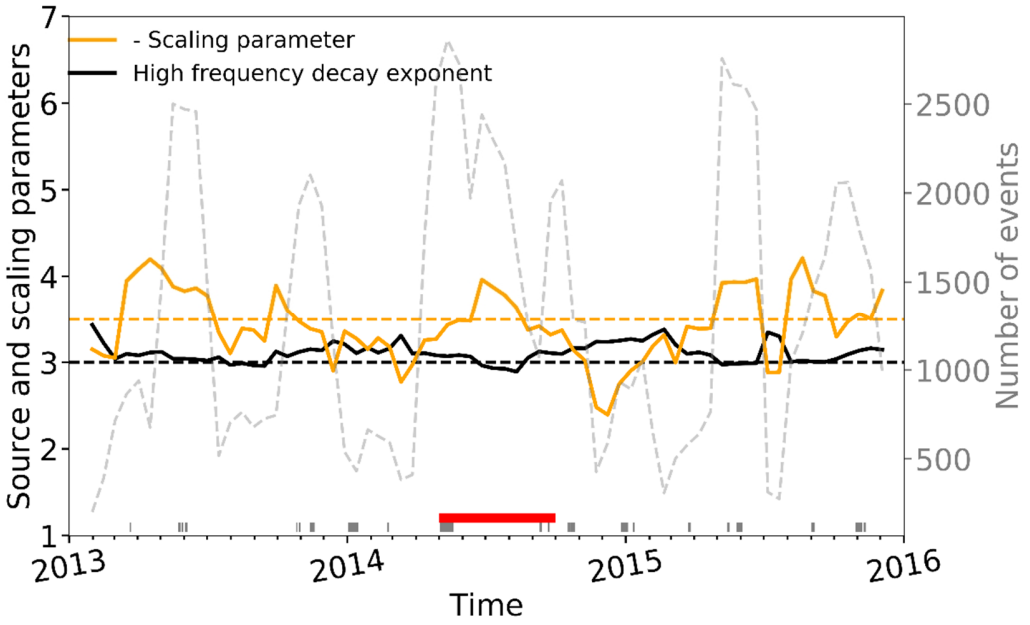

Figure 3. Time variation of source and scaling parameters. The scaling parameter *A'* (orange line) between corner frequency and seismic moment (see eq. (2)), and the high frequency source spectra decay exponent median value $\tilde{\gamma}$ (black line) are evaluated for the LFEs occurring in a 2-month moving time window, with a 15-day time-shift. The values fluctuate around the average value of the M_0-f_C scaling parameter and the median value of the high frequency decay exponent (orange and black horizontal dashed line, respectively) estimated for the whole three years analyzed (see Figure 2 and Figure S7). We do not observe a correlation with the number of events occurring in each selected time window (grey dotted line), which shows the time variation of rate of LFEs following the occurrence of short-term (grey horizontal bar) and long-term (red horizontal bar) SSEs in the explored region.

Variation in space of LFEs source characteristics can reveal change in physical properties along the subduction interface. We thus investigate along-strike variation of the estimated source parameters, thanks to the high spatial resolution of the LFE events provided by the automated detection-location method. We define six along-strike regions of LFE activity based on the binned distribution of the LFE counts along the strike distance during the whole 3-year period and on details of the LFE space-time activity (Figure 1c). Detailed information about the defined regions is summarized in Table S1.

We do not observe any spatially coherent variation of the moment-duration scaling parameter (Figure 4a), or of the high frequency decay exponents of the source spectra (Figure 4b). In addition,

here it is of our interest to investigate a possible variation of the scaling intercept B of eq. (2), since it could provide information on the variation of the effective strength of the interface between different along-strike regions. We fix the scaling parameter A' to the value -3, assuming that in each region the stress drop $\Delta\sigma$ and rupture velocity v_R are not varying with the seismic moment. This is the classical earthquake self-similarity, which is consistent with our scaling parameter estimation over the whole study area (see section 5.1). If A' = -3, the intercept B depends only on the effective static stress drop and rupture velocity of the selected along-strike region (see section 4). As such, variation of the intercept maps variation of $\Delta\sigma$ and v_R between different regions. This analysis reveals two levels of the scaling intercept characterizing the along-strike regions 1-3 and 4-6 (Figure 4c and Table S1). It is worth to note here that uncertainty in these estimations is quite small (absorbed by the circles dimension in Figure 4c), as a result of the linear regression with only one free parameter.

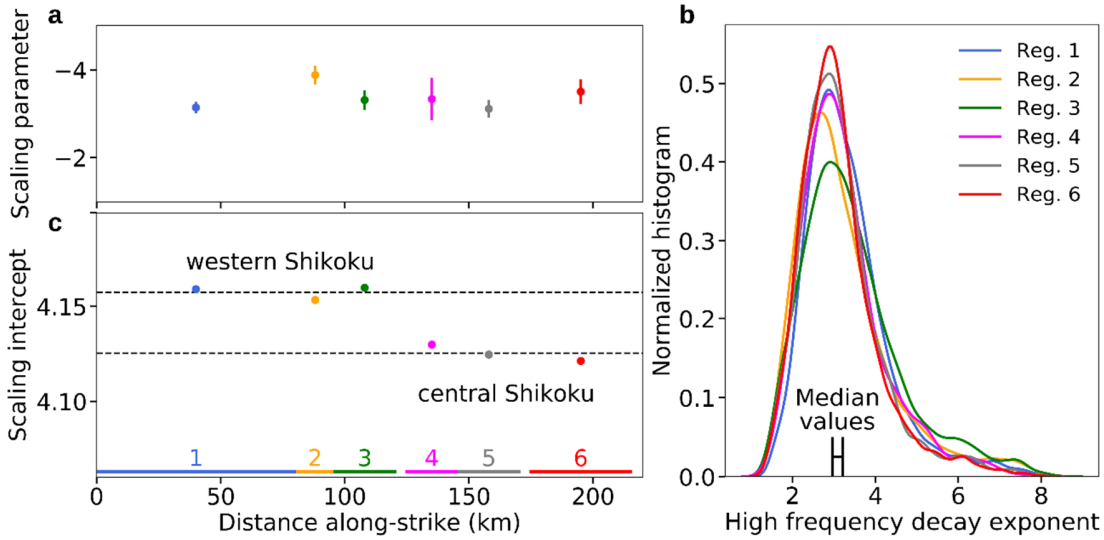

Figure 4. Along strike variation of source parameters. **a,** The scaling parameter A' (colored circles) between corner frequency and seismic moment (see eq. (2)) estimated for the LFEs occurring in defined along-strike regions (colored horizontal bars). **b,** Normalized histogram (density) of high frequency decay exponents for each selected region (see key); the black segment shows the median values range for all the distributions (2.97 – 3.21). **c,** The scaling intercept B (colored circles) of the scaling between corner frequency and seismic moment (see eq. (2)) is estimated for each selected region (colored horizontal bars), fixing A' = -3 (see eq. (3)); we distinguish two intercept levels (horizontal dashed lines) for western and central Shikoku. The error bars are too small to be visualized (see Table S1). Colors referred to the different along-strike regions, see Table S1.

Both $\Delta\sigma$ and v_R are expected to be smaller for weaker material interface, leading to a smaller B value. As such, the observed along-strike variation of the intercept B could be the signature that the subduction material interface beneath the central Shikoku region is mechanically weaker than beneath western Shikoku. To go further and estimate the effective static stress drop and rupture velocity values from the observed intercept, one needs to assume a specific source expansion model. However, since $\Delta\sigma$ and v_R are correlated (e.g., Causse & Song, 2015; Chounet et al., 2018; Supino et al., 2020) and independent estimations are not available, we can only estimate the value of one by fixing the other in a parametric analysis of eq. (3). Following previous results of Supino

et al. (2020), assuming the constant effective rupture velocity v_R to be 10% of the shear-wave velocity, and the circular rupture model of Sato and Hirasawa (1973), the k coefficient in eq. (3) and (5) is equal to 0.096. Then, assuming a shear-wave velocity β = 3.7 km s^{-1}, from eq. (3) we estimate an effective static stress drop $\overline{\Delta\sigma}$ = 29.0 kPa in the western along-strike region whereas in the central region $\overline{\Delta\sigma}$ = 23.2 kPa. It is worth to note that the ratio between the two stress drop levels, which is equal to 1.25, does not depend on the assumed rupture velocity as long as it remains constant.

On the other hand, assuming a constant effective stress drop in the different along-strike regions, variation of the effective rupture velocity may explain the along-strike variation of the intercept value. Assuming $\overline{\Delta\sigma}$ = 29.0 kPa and β = 3.7 km s^{-1}, from eq. (3) we evaluate k = 0.089 in the central region leading to a rupture speed 17% lower than the one in the western region (k = 0.096, v_R = 10% β).

5.2.1 Aftershocks' contamination in the automatic LFE catalog

The analysis of time variation of the source parameters allows detecting possible strong aftershocks' contamination in the automated output of the LFE detection method due to main events occurring during the year 2016 (Figure S9). The variation in time of the moment-duration scaling parameter clearly shows two peaks following the occurrence of the Kumamoto earthquake (M 7.0, April 16th, 2016) and the Tottori earthquake (M 6.6, October 21st, 2016) (Figure S9a). During the same period, we do not observe a similar variation when analyzing the JMA LFE catalog (Figure S9b). The higher scaling parameters are due to anomalous events, with large seismic moment and corresponding corner frequency larger than what is usually observed for other time intervals. Specifically, during the time period following the Kumamoto earthquake (April, 1st 2016 – June, 1st 2016), characterized by the highest scaling parameter (5.96), we observe 58 events with log M_0 > 12.0 and f_C > 2.0 Hz (Figure S9c), while the average number of such events is 8.2 during non-contaminated time windows. We visually inspected the waveforms corresponding to those detections, finding that 75% of them were false detections (red circles in Figure S9c), as shown in Figure S9d. The misidentification of a part of the P-wave of a ~200 km distant aftershock (M 3.5, JMA event-ID J2016041603520190), wrongly interpreted as the S-wave of a closer event (~40 km), leads to a false LFE detection by the automatic method. As such, the estimated source parameters are biased by the false hypocentral distance, wave-type and selected time window. For these reasons, we decided to exclude the year 2016 in this study. These observations might help to better design criteria and processing steps in the automatic detection method to avoid such spurious effects. However, this deserves further investigation and is beyond the scope of this study.

5.3 Event size distribution

A large number of world-wide observations (Kagan, 1999) shows that recurrence of regular earthquakes is well described by the Gutenberg-Richter (G-R) law (Gutenberg & Richter, 1944) that provides a statistical relationship between the magnitude M and total number N of earthquakes exceeding this magnitude:

$$\log N = a - bM , \qquad (6)$$

where a is a normalization constant depending on the analyzed catalog and b (the so-called b-value) is generally ranging from 0.5 to 2 (e.g., El-Isa & Eaton, 2014). Converting the magnitude into seismic moment M_0, this law can be re-written as:

$$N = \alpha M_0^{-\beta}, \quad (7)$$

where α is a normalization constant depending on the catalog analyzed and $\beta = 2/3\ b$. Therefore, the G-R distribution is often referenced as a power-law. The G-R distribution does not have a well-defined mean (nor a finite variance) and is a clear manifestation of scale invariance in the occurrence of earthquakes. This implies that earthquakes do not have a characteristic size and that the probability of their occurrence is proportional to the area of the ruptured fault (e.g., Rundle, 1989).

When characteristic scales appear in the problem, such as lower and upper size cut-offs, the concept of scale-invariance ceases and the original scale invariant law is modulated by functions involving non-dimensional factor built with these new scales. This leads to moment distributions with clear characteristic values. Such type of distribution has been reported for volcanic long-period seismicity and interpreted as the signature of scale-dependent fluid-related processes (e.g., Galina et al., 2020; Lahr et al., 1994; Melnik et al., 2020). At much smaller scale, the size distribution of dislocations in plastically deforming materials is shown to be controlled by internal disorder-related length scales, introducing lower size cut-offs that lead to distributions with characteristic values (Zhang et al., 2017). Finite size invariance has been also observed for regular earthquakes. Seismogenic zones, limited by the size of the brittle part of the crust or by quench heterogeneity and long-range elastic interactions leading to seismically coupled segments along fault and subduction interfaces, imply that the occurrence of earthquakes above a certain size becomes very unlikely. This upper cut-off of the scale invariance can be modeled as a Tapered Gutenberg-Richter (TGR) distribution (Kagan, 2002; Verejones et al., 2001). On the other hand, observed tapering of the G-R distribution at small magnitudes is often attributed to lower cut-offs that can be associated to context-dependent detectability limits of very small earthquakes leading to incomplete catalogs. Rundle (1993) also argued that detection limits cannot fully account for the observed reduction of the number of small earthquakes relative to the G-R law. He proposed that lower cut-off at small magnitudes could be also associated to a characteristic size scale such as the finite width of the inelastic fault zone.

5.3.1 Data selection and analysis

We analyze the LFE size distribution and its possible non-G-R behavior. The fully automated approach designed in this study aims to reliably investigate the distribution, reducing the probability of having missed or false events. In the LFE detection step, we analyze the raw, continuous signals with one major *a-priori* assumption: the frequency range (2.0-15.0 Hz) in which LFEs are expected to have the largest information content (Obara & Hirose, 2006) (see section 2). No *a-priori* assumptions are made on the waveform shape or on the location of the events to be detected, differently from matched-filter detection techniques. The massive output coming from this step should restrain the number of missing detections. Events are thus mainly selected through the analysis of their signal-to-noise ratios, discarding detections for which the information carried by the signal is almost indistinguishable from that carried by the noise (see section 3.1). This stage should allow to reduce possible false detections. Finally, source parameters PDFs are evaluated using again raw, unfiltered signals, and the inferred seismic moment distribution is analyzed in this section.

5.3.2 Observed event size distribution

The observed LFEs size distribution is presented in Figure 5. Figure 5a shows a normalized histogram of estimated seismic moments M_0 and its approximation by a normal distribution. Figure 5b-d show a more "standard" representation where the number of events exceeding a certain magnitude (log M_0) is plotted. This cumulative curve is then fitted with bounded G-R distributions described in Appendix A. The observed event size distribution is very well fitted with a normal distribution and also can be reasonably fitted with left and right bounded G-R distributions. This shape of the observed distribution would be in agreement with a scale limited or bounded process generating the observed LFEs. For seismic moment, a characteristic value can be inferred from the maximum of the best-fit normal distribution, log M_0^* = 11.36. This value corresponds to a bin-averaged corner frequency f_C^* = 2.4 ± 0.8 Hz (see Figure 2). From eq. (5), assuming k = 0.096 (corresponding to $v_R = 0.1\beta$ and a stress drop level ~30 kPa, see Supino et al. (2020)) and β = 3.7 km s^{-1}, this would imply a characteristic source size r^* = 150 ± 50 m. These results are very close to the results of Chestler and Creager (2017) who reported a scale-limited source process for LFEs beneath the Olympic Peninsula in the Cascadia subduction zone with a characteristic log M_0 = 11.3 from which they deduced typical LFEs source diameter close to 200~300 m. Such characteristic length scales can be related to the finite width of the deformed shear zone associated with the slow slipping parts of the faults (e.g., Angiboust et al., 2015) Alternatively, the observed event size distribution could indicate the existence of some characteristic disorder-related scale (block size) in ophiolite mélanges (e.g., Federico et al., 2007).

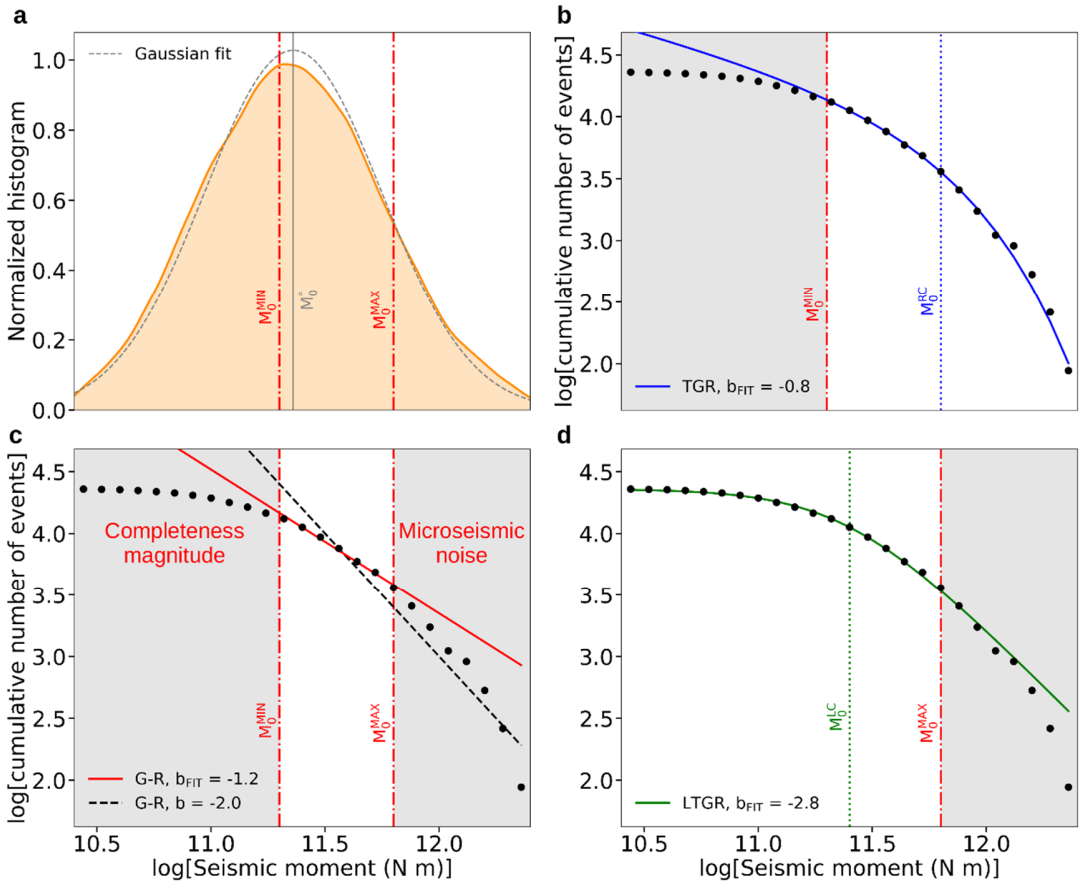

Figure 5. Observed event size distribution and fit of possible models. Grey rectangles show the biased event counts excluded in each fit. **a,** Normalized histogram (density) of log M_0 estimates,

together with the estimated bounds of the complete seismic moment domain (red dash-dotted vertical lines), outside which it is highly likely to have missing detections (see Figures S10 and S11). Grey dashed curve shows a best fit normal distribution with average log M_0^* = 11.36 (grey vertical line) and standard deviation σ = 0.39. **b,** Fit of cumulative number of events using eq. (A2) (TGR distribution), for log M_0 > log M_0^{MIN} (red dash-dotted line). The estimated right corner moment log M_0^{RC} (blue dotted line) is coincident with log M_0^{MAX}, the moment beyond which we have missing detections mainly due to microseismic noise. **c,** Fit of cumulative number of events using eq. (A1) (G-R distribution), for log M_0^{MIN} < log M_0 < log M_0^{MAX}, "safe" domain without missing samples. The estimated *b*-value is 1.2. **d,** Fit of cumulative number of events using eq. (A3) (LTGR distribution), for log M_0 < log M_0^{MAX} (red dash-dotted line). The estimated left corner moment log M_0^{LC} = 11.4 (green dotted line) is very close to log M_0^{MIN} = 11.3, network-related completeness seismic moment.

5.3.3 Maximum and minimum (completeness) seismic moment

The results presented in the previous subsection might be affected by the incompleteness of the analyzed LFE catalog. To identify possibly missed events in the observed size distribution, we start investigating the corner frequency distribution in each seismic moment bin used for event counts (Figure S10). Corner frequencies are normally distributed for log M_0 bins varying from 10.4 to 11.8. Beyond this seismic moment, a truncation effect is clearly observed for corner frequencies below 1 Hz. Thus, we define log $M_0^{MAX} \equiv 11.8$ as the maximum seismic moment of the "safe", complete domain. We suspect that missing samples occur due to two reasons: (1) secondary microseismic noise, which arises at frequencies below 1 Hz (e.g., Gualtieri et al., 2015; Hasselmann, 1963; Webb, 1998); (2) the vicinity of the minimum frequency used in the spectral inversion (0.7 Hz, defined by the instrumental response function), that strongly limits the available bandwidth on the left of f_C (Supino et al., 2019).

Close to the lower limit of the explored seismic moments, we still observe normal-like distributions of the corner frequency. Nevertheless, this is not enough to conclude that the completeness seismic moment (log M_0^{MIN}) is lower than the observed minimum (log M_0 = 10.4). Missing detections due to low signal-to-noise ratio (SNR) might be almost uniformly distributed in the bin. This would not significantly affect the shape of the corner frequency distributions at M_0 lower than M_{MIN}, but would introduce a biased in the total number of events in the bin.

To conservatively estimate M_{MIN}, we use the results of Schorlemmer et al. (2018) who evaluated the earthquake detection probabilities in Japan using a network-based method (Schorlemmer & Woessner, 2008). They estimated the completeness magnitude M_C for each node of a 0.2° × 0.2° grid that covers the all Japan. Depth layers vary between 0, 30, 100 and 500 km. Temporal variations in the JMA network detection capabilities are taken into account by updating their estimates each month. According to their results M_C varies between -1.0 and 5.0. The M_C value of the grid node closest to an earthquake location represents the best estimate of the completeness magnitude of the network, given that specific location. It is worth to note that unlike different, catalog-based, methods such as the maximum-curvature method (e.g., Wiemer & Wyss, 2000), Schorlemmer et al. (2018) estimates do not assume a G-R distribution.

We consider the M_C values computed by Schorlemmer et al. (2018) for December, 2012 and a depth of 30 km corresponding to the average depth of our catalog. Consequently, we obtain the M_C distribution selecting the node closest to each LFE location (Figure S11a); the median of the distribution is M_C^* = 0.2 (64% of the samples). In order to define log M_0^{MIN}, we have to convert M_C^* – which is calibrated on the JMA magnitude scale – in seismic moment units. To perform the

conversion, we select all the processed JMA events (Figure S2) having a JMA magnitude equal to 0.2, and analyze the corresponding seismic moment estimates (Figure S11b). The distribution is normal-like, and we define as completeness seismic moment the lower bound of the 68% confidence interval: $\log M_0^{MIN} \equiv 11.3$.

The analysis of the LFE catalog completeness results in a very narrow band of magnitudes (logarithms of seismic moment). This implies that possible results in the analysis of the event-size distribution should be taken very cautiously. So far, the characteristic value of the seismic moment that could be inferred from the normal distribution ($\log M_0^* = 11.36$) is very close to the lower completeness limit $\log M_0^{MIN}$ (Figure 5a). Moreover, corner moments $\log M_0^{LC}$ and $\log M_0^{RC}$ inferred from bounded, left and right tapered, G-R distributions (see Appendix A) are very close or coincide with the completeness limits $\log M_0^{MIN}$ and $\log M_0^{MAX}$ (Figure 5b,d). This suggests that the observed corner moments, which in principle could lead to a physical interpretation in terms of minimum of maximum possible length scales, are indeed closely related to the observational limits of this study. Finally, the observed distribution taken exactly within the established completeness limits can be reasonably fit by a G-R distribution with $b = 1.2$ (Figure 5b). This shows that a simple analysis within the narrow completeness band cannot distinguish between scale bounded (limited) and scale invariant behavior of the LFE sources in Shikoku. Developing a more sophisticated statistical analysis of the event occurrence accounting for more accurate noise models to assess missed detections would be required to advance in this direction. Such complex analysis is, however, out of scope of the present paper. At the same time, developing it in the future might be very important for improving physical understanding of LFE source processes because the catalog incompleteness reported here may not be specific of the Shikoku region but also affect LFE observations in other regions of the World.

6. Discussion and conclusions

In this work, we estimate the joint PDF of the source parameters of ~23,000 LFEs automatically detected during three years (2013-2015) in western and central Shikoku (Figure 1). We find a scaling parameter between seismic moment and corner frequency equal to -3.5 ± 0.8 (Figure 2a, Figure S7a), consistent with the -3 scaling of regular earthquakes (Aki, 1967), and an omega-cube high-frequency decay of the LFE spectra (Figure 2b), in contrast to the omega-squared power law observed for fast, ordinary earthquakes (Madariaga, 1976). While a cubic LFE moment-duration scaling suggests self-similarity, as observed for regular earthquakes, with a stress drop independent of the event size (Abercrombie, 1995; Allmann & Shearer, 2009), a cubic high-frequency decay may suggest different, smoother arrest phase for LFEs rupture process (Boatwright, 1980) when compared to regular earthquakes.

The estimated mean value of the scaling parameter (-3.5) is different from -3, although it remains consistent within one standard deviation. A truncation effect observed for seismic moments larger than $10^{11.8}$ N m and corner frequencies below 1 Hz (Figure S10) might be the cause of this difference. Indeed, evaluating the scaling parameter PDF for $\log M_0 \leq 11.8$, the distribution exhibits a mode equal to -3 (Figure S7b) while the median value of the high-frequency source spectra decay exponents does not change.

Our study benefits from a continuous automated LFE catalog, extended when compared with previous similar observations in the same region (Supino et al., 2020). The detailed time-resolution of the catalog allows us to investigate the related source parameters variability and assess the robustness of the results. We find that the parameters of both the moment-duration scaling and the

high-frequency decay of the LFE source spectra are stable in time, without any significant variation correlated with the observed changes in LFEs activity (Figure 3) in relation with short-term or long-term SSEs. Additionally, we validated our results by estimating the source parameters for a different LFE dataset, composed of ~3000 events manually detected by JMA in the same region and within the same time interval of our automated catalog. Results for the two catalogs are shown to be very similar (Figure S2).

We also take advantage of the spatial resolution of our data (LFE catalog), exploring possible along-strike variations of the physical properties along the subduction material interface through the analysis of the intercept coefficient of the seismic moment – corner frequency scaling (see section 4 and Figure 4). We observe a spatially coherent variation of the intercept, with two different levels for the western and central Shikoku along-strike regions (Figure 4). If a constant rupture velocity is assumed, those levels correspond to different static stress-drop levels for the western (higher stress drop) and the central (lower stress drop) along-strike regions, with a ratio of 1.25. Alternatively, assuming a constant static stress drop we estimate an effective rupture velocity in the central along-strike region that is 17% lower than in the western along-strike region. In both cases, this result suggest the existence of a mechanically stronger (western) and a mechanically weaker (central) patch in Shikoku. Kano et al. (2018) also revealed strength variation of tremor patches in Shikoku, modeling tremor and SSE activity. However, in their study the weaker patch lies in a different area, corresponding to our along-strike regions 2 and 3 (Figure 4 and Table S1).

The along-strike discontinuity that we find for the intercept coefficient overlaps the gap that we observe in the spatial distribution of detected LFEs (Figure 1). Interestingly, this gap corresponds to an almost constant value (T ~400 °C) in the temperature distribution calculated by Ji et al. (2016) close to the LFE source region, while T increases (up to ~700 °C) moving to both the western and central regions (see Figure 11e in Ji et al. (2016)), where most of the LFE activity is detected. Ji et al. suggested a possible interpretation in terms of fluid-enhanced LFE activity in relation with the temperature gradient, eventually associated to the phase transformations of hydrous minerals in the mid-ocean ridge basalt (MORB) of the subducting slab.

Finally, we analyze the LFE size distribution (Figure 5). The results in the entire observed seismic moment domain ($\log M_0 = 10.4 – 12.4$) cannot be explained with a G-R law and require considering finite size invariance, with scale bounded or tapered distributions. This analysis results in a characteristic value of the seismic moment $\log M_0^* = 11.3$~11.4 corresponding to an LFE source size of 150~200 m. Such characteristic length scale could be related either to the finite width of the deformed shear zone associated with the slow slipping parts of the interface or to the existence of some characteristic disorder-related scale (block size) in these deformed zones.

However, when investigating possible bias in the event counts, we find that the analyzed LFE catalog is only complete in a very narrow range of seismic moments: $11.3 < \log M_0 < 11.8$ (Figures S10 and S11). Network-related completeness magnitude and secondary microseisms seem to be the cause of the missing event detections in the left and right bins, resulting in the observed tapering. Corresponding corner moments estimated from the fit of the event size distribution are closely related to these observational limits (Figure 5). When analyzing the distribution in the narrow band of the catalog completeness, the scale bounded (limited) and scale invariant behaviors cannot be distinguished; a G-R with a b-value = 1.2 reasonably fits the observations in this range of seismic moments.

Nevertheless, we emphasize the need to assess possible missed events when analyzing and modeling the size distribution of LFEs: the collection of different results reported in the previous studies (see section 1) might just reflect our observational limits and unbalanced catalogs. Indeed,

the seismic moment range of reported world-wide LFEs detection is ~ 10^{10} – 10^{13} N m (Bostock et al., 2015; Chestler & Creager, 2017; Fletcher & McGarr, 2011; Ide, Shelly, et al., 2007), similarly to our estimates ($10^{10.4}$ – $10^{12.4}$ N m). Our results show that the maximum of this range might be related to secondary microseismic noise; therefore, detecting LFEs beyond this limit could be *a priori* extremely difficult. Regarding the lower bound, in principle, a seismic network with a better detection capability than the Hi-net in Japan could allow to detect LFEs with lower seismic moment, if those occur. Alternatively, more advanced methods for studying the LFE occurrence and detections accounting for the noise statistics should be developed to extend the analysis beyond the simple catalog completeness limits.

Appendix A: Analytical representation of event size distribution

We recall the analytical formulation of the G-R and TGR distributions using the cumulative complementary distribution function (CCDF) $\Phi(M_0)$, defined as a function of the seismic moment M_0. The CCDF $\Phi(M_0)$ multiplied by the total number of events N_{TOT} gives the expected cumulative number of events.

The G-R distribution has the following CCDF:

$$\Phi(M_0) = \left(\frac{M_0^{MIN}}{M_0}\right)^{\beta} \qquad \text{(A1)}$$

where M_0^{MIN} is the completeness seismic moment, i.e. the value below which the earthquake detection capability of the considered network, due to low signal-to-noise ratio, is no more uniform in space and time; β is equal to 2/3 of the *b*-value, the so-called power law exponent of the G-R law defined as a function of the magnitude.

The TGR distribution is defined by the following CCDF:

$$\Phi(M_0) = \left(\frac{M_0^{MIN}}{M_0}\right)^{\beta} \exp\left(\frac{M_0^{MIN} - M_0}{M_0^{RC}}\right) \qquad \text{(A2)}$$

Where M_0^{RC} is the right corner seismic moment, which parameterizes the upper cut-off of the distribution; M_0^{MIN} is the completeness seismic moment.

In addition to the previous well-known distributions, following Zhang et al. (2017) we define the Left Tapered Gutenberg-Richter distribution (LTGR) using the following CCDF:

$$\Phi(M_0) = \frac{1}{1+\left(M_0/M_0^{LC}\right)^{\beta}} \qquad \text{(A3)}$$

where M_0^{LC} is the left corner seismic moment, the parameter we use to introduce a lower cut-off for the G-R distribution.

We show in Figure A1 the expected cumulative number of events for the G-R, TGR and LTGR distributions. The TGR and LTGR distributions match the G-R distribution when $M_0 \ll M_0^{RC}$ and $M_0 \gg M_0^{LC}$, respectively.

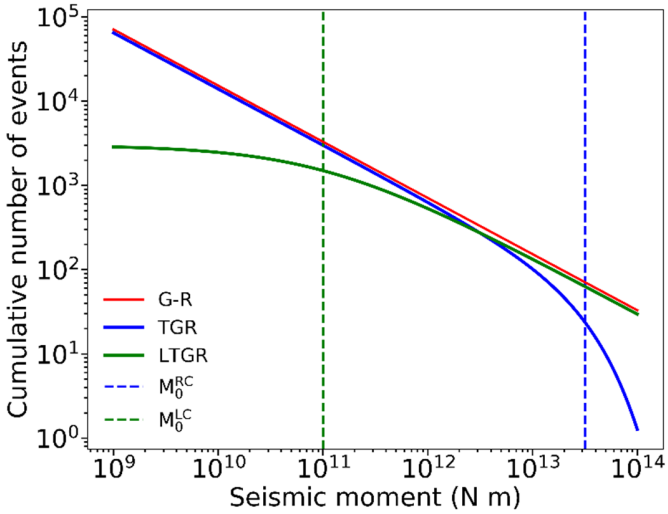

Figure A1. Expected cumulative number of events for the G-R, TGR, and LTGR event size distributions: the G-R distribution (red line, see eq. (A1)), TGR distribution ((blue line, see eq. (A2)) and LTGR distribution (green line, see eq. (A3)) are shown, together with the right corner moment M_0^{RC} of the TGR function (blue dashed vertical line) and the left corner moment M_0^{LC} of the LTGR function (green dashed vertical line). The TGR and LTGR functions converge to the G-R function when $M_0 \ll M_0^{RC}$ and $M_0 \gg M_0^{LC}$, respectively. Distributions parameters: G-R, b = 1.0; TGR, b = 1.0, log M_0^{RC} = 13.5; LTGR, b = 1.0, log M_0^{LC} = 11.0.

Acknowledgments
This study was supported by the European Research Council under the European Union Horizon 2020 research and innovation program (grant agreement no. 787399 - SEISMAZE) and by the Russian Ministry of Education and Science (Grant 14.W03.31.0033). Most numerical computations were performed on the S-CAPAD platform, at Institut de Physique du Globe de Paris (IPGP), France.

References

Abercrombie, R. E. (1995). Earthquake source scaling relationships from −1 to 5 M L using seismograms recorded at 2.5-km depth. *Journal of Geophysical Research: Solid Earth*, *100*(B12), 24015–24036. https://doi.org/10.1029/95JB02397

Abercrombie, R. E. (2015). Investigating uncertainties in empirical Green's function analysis of earthquake source parameters. *Journal of Geophysical Research: Solid Earth*, *120*(6), 4263–4277. https://doi.org/10.1002/2015JB011984

Abercrombie, R. E. (2021). Resolution and uncertainties in estimates of earthquake stress drop and energy release. *Philosophical Transactions of the Royal Society A: Mathematical, Physical and Engineering Sciences*, *379*(2196), 20200131. https://doi.org/10.1098/rsta.2020.0131

Aki, K. (1967). Scaling law of seismic spectrum. *Journal of Geophysical Research*. https://doi.org/10.1029/jz072i004p01217

Allmann, B. P., & Shearer, P. M. (2009). Global variations of stress drop for moderate to large earthquakes. *Journal of Geophysical Research: Solid Earth*, *114*(B1). https://doi.org/10.1029/2008JB005821

Angiboust, S., Kirsch, J., Oncken, O., Glodny, J., Monié, P., & Rybacki, E. (2015). Probing the transition between seismically coupled and decoupled segments along an ancient subduction

interface. *Geochemistry, Geophysics, Geosystems*, *16*(6), 1905–1922. https://doi.org/10.1002/2015GC005776

Annoura, S., Obara, K., & Maeda, T. (2016). Total energy of deep low-frequency tremor in the Nankai subduction zone, southwest Japan. *Geophysical Research Letters*. https://doi.org/10.1002/2016GL067780

Aso, N., Ohta, K., & Ide, S. (2011). Volcanic-like low-frequency earthquakes beneath Osaka Bay in the absence of a volcano. *Geophysical Research Letters*. https://doi.org/10.1029/2011GL046935

Aso, N., Ohta, K., & Ide, S. (2013). Tectonic, volcanic, and semi-volcanic deep low-frequency earthquakes in western Japan. *Tectonophysics*. https://doi.org/10.1016/j.tecto.2012.12.015

Audet, P., Bostock, M. G., Christensen, N. I., & Peacock, S. M. (2009). Seismic evidence for overpressured subducted oceanic crust and megathrust fault sealing. *Nature*. https://doi.org/10.1038/nature07650

Behr, W. M., & Bürgmann, R. (2020). Whats down there? The structures, materials and environment of deep-seated tremor and slip. *EarthArXiv*. https://doi.org/10.31223/osf.io/tyzb9

Bernaudin, M., & Gueydan, F. (2018). Episodic Tremor and Slip Explained by Fluid-Enhanced Microfracturing and Sealing. *Geophysical Research Letters*. https://doi.org/10.1029/2018GL077586

Boatwright, J. (1980). A spectral theory for circular seismic sources; simple estimates of source dimension, dynamic stress drop, and radiated seismic energy. *Bulletin of the Seismological Society of America*.

Bostock, M. G., Thomas, A. M., Savard, G., Chuang, L., & Rubin, A. M. (2015). Magnitudes and moment-duration scaling of low-frequency earthquakes beneath southern Vancouver Island. *Journal of Geophysical Research: Solid Earth*. https://doi.org/10.1002/2015JB012195

Bostock, M. G., Thomas, A. M., Rubin, A. M., & Christensen, N. I. (2017). On corner frequencies, attenuation, and low-frequency earthquakes. *Journal of Geophysical Research: Solid Earth*, *122*(1), 543–557. https://doi.org/10.1002/2016JB013405

Brown, J. R., Beroza, G. C., Ide, S., Ohta, K., Shelly, D. R., Schwartz, S. Y., et al. (2009). Deep low-frequency earthquakes in tremor localize to the plate interface in multiple subduction zones. *Geophysical Research Letters*. https://doi.org/10.1029/2009GL040027

Brune, J. N. (1970). Tectonic stress and the spectra of seismic shear waves from earthquakes. *Journal of Geophysical Research*, *75*(26), 4997–5009. https://doi.org/10.1029/JB075i026p04997

Causse, M., & Song, S. G. (2015). Are stress drop and rupture velocity of earthquakes independent? Insight from observed ground motion variability. *Geophysical Research Letters*. https://doi.org/10.1002/2015GL064793

Chestler, S. R., & Creager, K. C. (2017). Evidence for a scale-limited low-frequency earthquake source process. *Journal of Geophysical Research: Solid Earth*. https://doi.org/10.1002/2016JB013717

Chouet, B. A. (1996). Long-period volcano seismicity: Its source and use in eruption forecasting. *Nature*. https://doi.org/10.1038/380309a0

Chounet, A., Vallée, M., Causse, M., & Courboulex, F. (2018). Global catalog of earthquake rupture velocities shows anticorrelation between stress drop and rupture velocity. *Tectonophysics*. https://doi.org/10.1016/j.tecto.2017.11.005

Cocco, M., Tinti, E., & Cirella, A. (2016). On the scale dependence of earthquake stress drop.

Journal of Seismology. https://doi.org/10.1007/s10950-016-9594-4

Cotton, F., Archuleta, R., & Causse, M. (2013). What is sigma of the stress drop? *Seismological Research Letters*. https://doi.org/10.1785/0220120087

Cruz-Atienza, V. M., Villafuerte, C., & Bhat, H. S. (2018). Rapid tremor migration and pore-pressure waves in subduction zones. *Nature Communications*. https://doi.org/10.1038/s41467-018-05150-3

El-Isa, Z. H., & Eaton, D. W. (2014). Spatiotemporal variations in the b-value of earthquake magnitude–frequency distributions: Classification and causes. *Tectonophysics*, *615–616*, 1–11. https://doi.org/10.1016/j.tecto.2013.12.001

Eshelby, J. D. (1957). The determination of the elastic field of an ellipsoidal inclusion, and related problems. *Proceedings of the Royal Society of London. Series A. Mathematical and Physical Sciences*, *241*(1226), 376–396.

Farge, G., Shapiro, N. M., & Frank, W. B. (2020). Moment-Duration Scaling of Low-Frequency Earthquakes in Guerrero, Mexico. *Journal of Geophysical Research: Solid Earth*. https://doi.org/10.1029/2019JB019099

Federico, L., Crispini, L., Scambelluri, M., & Capponi, G. (2007). Ophiolite mélange zone records exhumation in a fossil subduction channel. *Geology*, *35*(6), 499. https://doi.org/10.1130/G23190A.1

Fehler, M. (1983). Observations of volcanic tremor at Mount St. Helens Volcano (US). *Journal of Geophysical Research*. https://doi.org/10.1029/JB088iB04p03476

Fletcher, J. B., & McGarr, A. (2011). Moments, magnitudes, and radiated energies of non-volcanic tremor near Cholame, CA, from ground motion spectra at UPSAR. *Geophysical Research Letters*, *38*(16), n/a-n/a. https://doi.org/10.1029/2011GL048636

Frank, W. B., Shapiro, N. M., Husker, A. L., Kostoglodov, V., Bhat, H. S., & Campillo, M. (2015). Along-fault pore-pressure evolution during a slow-slip event in Guerrero, Mexico. *Earth and Planetary Science Letters*. https://doi.org/10.1016/j.epsl.2014.12.051

Frank, William B. (2016). Slow slip hidden in the noise: The intermittence of tectonic release. *Geophysical Research Letters*. https://doi.org/10.1002/2016GL069537

Frank, William B., & Brodsky, E. E. (2019). Daily measurement of slow slip from low-frequency earthquakes is consistent with ordinary earthquake scaling. *Science Advances*. https://doi.org/10.1126/sciadv.aaw9386

Frank, William B., Shapiro, N. M., Kostoglodov, V., Husker, A. L., Campillo, M., Payero, J. S., & Prieto, G. A. (2013). Low-frequency earthquakes in the Mexican sweet spot. *Geophysical Research Letters*. https://doi.org/10.1002/grl.50561

Frank, William B., Shapiro, N. M., Husker, A. L., Kostoglodov, V., Romanenko, A., & Campillo, M. (2014). Using systematically characterized low-frequency earthquakes as a fault probe in Guerrero, Mexico. *Journal of Geophysical Research: Solid Earth*. https://doi.org/10.1002/2014JB011457

Frank, William B., Rousset, B., Lasserre, C., & Campillo, M. (2018). Revealing the cluster of slow transients behind a large slow slip event. *Science Advances*. https://doi.org/10.1126/sciadv.aat0661

Galina, N. A., Shapiro, N. M., Droznin, D. V., Droznina, S. Y., Senyukov, S. L., & Chebrov, D. V. (2020). Recurrence of Deep Long-Period Earthquakes beneath the Klyuchevskoi Volcano Group, Kamchatka. *Izvestiya, Physics of the Solid Earth*, *56*(6), 749–761. https://doi.org/10.1134/S1069351320060026

Ghosh, A., Huesca-Pérez, E., Brodsky, E., & Ito, Y. (2015). Very low frequency earthquakes in

Cascadia migrate with tremor. *Geophysical Research Letters*. https://doi.org/10.1002/2015GL063286

Gomberg, J., Wech, A., Creager, K., Obara, K., & Agnew, D. (2016). Reconsidering earthquake scaling. *Geophysical Research Letters*, *43*(12), 6243–6251. https://doi.org/10.1002/2016GL069967

Gualtieri, L., Stutzmann, E., Capdeville, Y., Farra, V., Mangeney, A., & Morelli, A. (2015). On the shaping factors of the secondary microseismic wavefield. *Journal of Geophysical Research: Solid Earth*. https://doi.org/10.1002/2015JB012157

Gutenberg, B., & Richter, C. F. (1944). Frequency of earthquakes in California*. *Bulletin of the Seismological Society of America*, *34*(4), 185–188.

Hanks, T. C., & Wyss, M. (1972). The use of body-wave spectra in the determination of seismic-source parameters. *Bulletin of the Seismological Society of America*.

Harrington, R. M., & Benson, P. M. (2011). Analysis of laboratory simulations of volcanic hybrid earthquakes using empirical Green's functions. *Journal of Geophysical Research: Solid Earth*. https://doi.org/10.1029/2011JB008373

Hasselmann, K. (1963). A statistical analysis of the generation of microseisms. *Reviews of Geophysics*. https://doi.org/10.1029/RG001i002p00177

Hiramatsu, Y., Watanabe, T., & Obara, K. (2008). Deep low-frequency tremors as a proxy for slip monitoring at plate interface. *Geophysical Research Letters*. https://doi.org/10.1029/2008GL034342

Hirose, H., Hirahara, K., Kimata, F., Fujii, N., & Miyazaki, S. (1999). A slow thrust slip event following the two 1996 Hyuganada earthquakes beneath the Bungo Channel, southwest Japan. *Geophysical Research Letters*. https://doi.org/10.1029/1999GL010999

Ide, S. (2014). Modeling fast and slow earthquakes at various scales. *Proceedings of the Japan Academy, Series B*, *90*(8), 259–277. https://doi.org/10.2183/pjab.90.259

Ide, S. (2016). Characteristics of slow earthquakes in the very low frequency band: Application to the Cascadia subduction zone. *Journal of Geophysical Research: Solid Earth*, *121*(8), 5942–5952. https://doi.org/10.1002/2016JB013085

Ide, S., & Yabe, S. (2014). Universality of slow earthquakes in the very low frequency band. *Geophysical Research Letters*. https://doi.org/10.1002/2014GL059712

Ide, S., Beroza, G. C., Shelly, D. R., & Uchide, T. (2007). A scaling law for slow earthquakes. *Nature*. https://doi.org/10.1038/nature05780

Ide, S., Shelly, D. R., & Beroza, G. C. (2007). Mechanism of deep low frequency earthquakes: Further evidence that deep non-volcanic tremor is generated by shear slip on the plate interface. *Geophysical Research Letters*. https://doi.org/10.1029/2006GL028890

Ito, Y., Obara, K., Shiomi, K., Sekine, S., & Hirose, H. (2007). Slow earthquakes coincident with episodic tremors and slow slip events. *Science*. https://doi.org/10.1126/science.1134454

Ito, Y., Obara, K., Matsuzawa, T., & Maeda, T. (2009). Very low frequency earthquakes related to small asperities on the plate boundary interface at the locked to aseismic transition. *Journal of Geophysical Research: Solid Earth*. https://doi.org/10.1029/2008JB006036

Ji, Y., Yoshioka, S., & Matsumoto, T. (2016). Three-dimensional numerical modeling of temperature and mantle flow fields associated with subduction of the Philippine Sea plate, southwest Japan. *Journal of Geophysical Research: Solid Earth*, *121*(6), 4458–4482. https://doi.org/10.1002/2016JB012912

Kagan, Y. Y. (1999). Universality of the Seismic Moment-frequency Relation. *Pure and Applied Geophysics*, *155*(2–4), 537–573. https://doi.org/10.1007/s000240050277

Kagan, Y. Y. (2002). Seismic moment distribution revisited: I. Statistical results. *Geophysical Journal International*, *148*(3), 520–541. https://doi.org/10.1046/j.1365-246x.2002.01594.x

Kanamori, H., & Anderson, D. L. (1975). Theoretical basis of some empirical relations in seismology. *Bulletin of the Seismological Society of America*, *65*(5), 1073–1095.

Kanamori, H., & Rivera, L. (2004). Static and dynamic scaling relations for earthquakes and their implications for rupture speed and stress drop. *Bulletin of the Seismological Society of America*. https://doi.org/10.1785/0120030159

Kaneko, Y., & Shearer, P. M. (2014). Seismic source spectra and estimated stress drop derived from cohesive-zone models of circular subshear rupture. *Geophysical Journal International*, *197*(2), 1002–1015. https://doi.org/10.1093/gji/ggu030

Kaneko, Y., & Shearer, P. M. (2015). Variability of seismic source spectra, estimated stress drop, and radiated energy, derived from cohesive-zone models of symmetrical and asymmetrical circular and elliptical ruptures. *Journal of Geophysical Research: Solid Earth*. https://doi.org/10.1002/2014JB011642

Kano, M., Aso, N., Matsuzawa, T., Ide, S., Annoura, S., Arai, R., et al. (2018). Development of a Slow Earthquake Database. *Seismological Research Letters*, *89*(4), 1566–1575. https://doi.org/10.1785/0220180021

Kano, M., Kato, A., Ando, R., & Obara, K. (2018). Strength of tremor patches along deep transition zone of a megathrust. *Scientific Reports*, *8*(1), 3655. https://doi.org/10.1038/s41598-018-22048-8

Kao, H., Shan, S. J., Dragert, H., Rogers, G., Cassidy, J. F., & Ramachandran, K. (2005). A wide depth distribution of seismic tremors along the northern Cascadia margin. *Nature*. https://doi.org/10.1038/nature03903

Kao, H., Wang, K., Dragert, H., Kao, J. Y., & Rogers, G. (2010). Estimating seismic moment magnitude (Mw) of tremor bursts in northern Cascadia: Implications for the "seismic efficiency" of episodic tremor and slip. *Geophysical Research Letters*. https://doi.org/10.1029/2010GL044927

Katsumata, A., & Kamaya, N. (2003). Low-frequency continuous tremor around the Moho discontinuity away from volcanoes in the southwest Japan. *Geophysical Research Letters*, *30*(1), 20-1-20–4. https://doi.org/10.1029/2002GL015981

Kubo, A., Fukuyama, E., Kawai, H., & Nonomura, K. (2002). NIED seismic moment tensor catalogue for regional earthquakes around Japan: Quality test and application. *Tectonophysics*. https://doi.org/10.1016/S0040-1951(02)00375-X

Lahr, J. C., Chouet, B. A., Stephens, C. D., Power, J. A., & Page, R. A. (1994). Earthquake classification, location, and error analysis in a volcanic environment: implications for the magmatic system of the 1989–1990 eruptions at redoubt volcano, Alaska. *Journal of Volcanology and Geothermal Research*, *62*(1–4), 137–151. https://doi.org/10.1016/0377-0273(94)90031-0

Lomax, A. (2005). A reanalysis of the hypocentral location and related observations for the great 1906 California earthquake. *Bulletin of the Seismological Society of America*, *95*(3), 861–877.

Lomax, A. (2008). Location of the focus and tectonics of the focal region of the California earthquake of 18 April 1906. *Bulletin of the Seismological Society of America*. https://doi.org/10.1785/0120060405

Madariaga, R. (1976). Dynamics of an expanding circular fault. *Bull. Seismol. Soc. Am.*

Maeda, T., & Obara, K. (2009). Spatiotemporal distribution of seismic energy radiation from low-

frequency tremor in western Shikoku, Japan. *Journal of Geophysical Research: Solid Earth*. https://doi.org/10.1029/2008JB006043

Maury, J., Ide, S., Cruz-Atienza, V. M., Kostoglodov, V., González-Molina, G., & Pérez-Campos, X. (2016). Comparative study of tectonic tremor locations: Characterization of slow earthquakes in Guerrero, Mexico. *Journal of Geophysical Research: Solid Earth*. https://doi.org/10.1002/2016JB013027

Maury, J., Ide, S., Cruz-Atienza, V. M., & Kostoglodov, V. (2018). Spatiotemporal Variations in Slow Earthquakes Along the Mexican Subduction Zone. *Journal of Geophysical Research: Solid Earth*. https://doi.org/10.1002/2017JB014690

Melnik, O., Lyakhovsky, V., Shapiro, N. M., Galina, N., & Bergal-Kuvikas, O. (2020). Deep long period volcanic earthquakes generated by degassing of volatile-rich basaltic magmas. *Nature Communications*, *11*(1), 3918. https://doi.org/10.1038/s41467-020-17759-4

Michel, S., Gualandi, A., & Avouac, J.-P. (2019). Similar scaling laws for earthquakes and Cascadia slow-slip events. *Nature*, *574*(7779), 522–526. https://doi.org/10.1038/s41586-019-1673-6

Nadeau, R. M., & Dolenc, D. (2005). Nonvolcanic tremors deep beneath the San Andreas Fault. *Science*. https://doi.org/10.1126/science.1107142

Nakamura, M., & Sunagawa, N. (2015). Activation of very low frequency earthquakes by slow slip events in the Ryukyu Trench. *Geophysical Research Letters*. https://doi.org/10.1002/2014GL062929

Nakano, M., Yabe, S., Sugioka, H., Shinohara, M., & Ide, S. (2019). Event Size Distribution of Shallow Tectonic Tremor in the Nankai Trough. *Geophysical Research Letters*. https://doi.org/10.1029/2019GL083029

Obara, K. (2002). Nonvolcanic deep tremor associated with subduction in southwest Japan. *Science*. https://doi.org/10.1126/science.1070378

Obara, K., & Hirose, H. (2006). Non-volcanic deep low-frequency tremors accompanying slow slips in the southwest Japan subduction zone. *Tectonophysics*. https://doi.org/10.1016/j.tecto.2005.04.013

Obara, K., & Ito, Y. (2005). Very low frequency earthquakes excited by the 2004 off Kii peninsula earthquakes: A dynamic deformation process in the large accretionary prism. *Earth, Planets and Space*. https://doi.org/10.1186/BF03352570

Obara, K., & Kato, A. (2016). Connecting slow earthquakes to huge earthquakes. *Science*, *353*(6296), 253–257. https://doi.org/10.1126/science.aaf1512

Obara, K., Tanaka, S., Maeda, T., & Matsuzawa, T. (2010). Depth-dependent activity of non-volcanic tremor in southwest Japan. *Geophysical Research Letters*. https://doi.org/10.1029/2010GL043679

Okada, Y., Kasahara, K., Hori, S., Obara, K., Sekiguchi, S., Fujiwara, H., & Yamamoto, A. (2004). Recent progress of seismic observation networks in Japan - Hi-net, F-net, K-net and KiK-net -. *Earth, Planets and Space*. https://doi.org/10.1186/BF03353076

Oth, A. (2013). On the characteristics of earthquake stress release variations in Japan. *Earth and Planetary Science Letters*. https://doi.org/10.1016/j.epsl.2013.06.037

Ozawa, S. (2017). Long-term slow slip events along the Nankai trough subduction zone after the 2011 Tohoku earthquake in Japan. *Earth, Planets and Space*. https://doi.org/10.1186/s40623-017-0640-4

Payero, J. S., Kostoglodov, V., Shapiro, N., Mikumo, T., Iglesias, A., Pérez-Campos, X., & Clayton, R. W. (2008). Nonvolcanic tremor observed in the Mexican subduction zone.

Geophysical Research Letters. https://doi.org/10.1029/2007GL032877

Poiata, N., Satriano, C., Vilotte, J. P., Bernard, P., & Obara, K. (2016). Multiband array detection and location of seismic sources recorded by dense seismic networks. *Geophysical Journal International*. https://doi.org/10.1093/gji/ggw071

Poiata, N., Vilotte, J. P., Bernard, P., Satriano, C., & Obara, K. (2018). Imaging different components of a tectonic tremor sequence in southwestern Japan using an automatic statistical detection and location method. *Geophysical Journal International*. https://doi.org/10.1093/gji/ggy070

Rogers, G., & Dragert, H. (2003). Episodic tremor and slip on the Cascadia subduction zone: The chatter of silent slip. *Science*. https://doi.org/10.1126/science.1084783

Rundle, J. B. (1989). Derivation of the complete Gutenberg-Richter magnitude-frequency relation using the principle of scale invariance. *Journal of Geophysical Research*, *94*(B9), 12337. https://doi.org/10.1029/JB094iB09p12337

Rundle, J. B. (1993). Magnitude-frequency relations for earthquakes using a statistical mechanical approach. *Journal of Geophysical Research: Solid Earth*, *98*(B12), 21943–21949. https://doi.org/10.1029/93JB02037

Sato, T., & Hirasawa, T. (1973). Body wave spectra from propagating shear cracks. *Journal of Physics of the Earth*. https://doi.org/10.4294/jpe1952.21.415

Savage, J. C. (1972). Relation of corner frequency to fault dimensions. *Journal of Geophysical Research*. https://doi.org/10.1029/jb077i020p03788

Schorlemmer, D., & Woessner, J. (2008). Probability of detecting an earthquake. *Bulletin of the Seismological Society of America*. https://doi.org/10.1785/0120070105

Schorlemmer, D., Hirata, N., Ishigaki, Y., Doi, K., Nanjo, K. Z., Tsuruoka, H., et al. (2018). Earthquake Detection Probabilities in Japan. *Bulletin of the Seismological Society of America*, *108*(2), 702–717. https://doi.org/10.1785/0120170110

Shapiro, N. M., Campillo, M., Kaminski, E., Vilotte, J. P., & Jaupart, C. (2018). Low-Frequency Earthquakes and Pore Pressure Transients in Subduction Zones. *Geophysical Research Letters*. https://doi.org/10.1029/2018GL079893

Shelly, D. R., Beroza, G. C., Ide, S., & Nakamula, S. (2006). Low-frequency earthquakes in Shikoku, Japan, and their relationship to episodic tremor and slip. *Nature*. https://doi.org/10.1038/nature04931

Shelly, D. R., Beroza, G. C., & Ide, S. (2007). Non-volcanic tremor and low-frequency earthquake swarms. *Nature*. https://doi.org/10.1038/nature05666

Supino, M., Festa, G., & Zollo, A. (2019). A probabilistic method for the estimation of earthquake source parameters from spectral inversion: application to the 2016–2017 Central Italy seismic sequence. *Geophysical Journal International*, *218*(2), 988–1007. https://doi.org/10.1093/gji/ggz206

Supino, M., Poiata, N., Festa, G., Vilotte, J. P., Satriano, C., & Obara, K. (2020). Self-similarity of low-frequency earthquakes. *Scientific Reports*, *10*(1), 6523. https://doi.org/10.1038/s41598-020-63584-6

Sweet, J. R., Creager, K. C., & Houston, H. (2014). A family of repeating low-frequency earthquakes at the downdip edge of tremor and slip. *Geochemistry, Geophysics, Geosystems*, *15*(9), 3713–3721. https://doi.org/10.1002/2014GC005449

Takahashi, T., Obana, K., Yamamoto, Y., Nakanishi, A., Kodaira, S., & Kaneda, Y. (2014). S wave attenuation structure on the western side of the Nankai subduction zone: Implications for fluid distribution and dynamics. *Journal of Geophysical Research: Solid Earth*, *119*(10),

7805–7822. https://doi.org/10.1002/2014JB011103

Verejones, D., Robinson, R., & Yang, W. (2001). Remarks on the accelarated moment release model: Problems of model formulation, simulation and estimation. *Geophysical Journal International*. https://doi.org/10.1046/j.1365-246X.2001.01348.x

Watanabe, T., Hiramatsu, Y., & Obara, K. (2007). Scaling relationship between the duration and the amplitude of non-volcanic deep low-frequency tremors. *Geophysical Research Letters*. https://doi.org/10.1029/2007GL029391

Webb, S. C. (1998). Broadband seismology and noise under the ocean. *Reviews of Geophysics*. https://doi.org/10.1029/97RG02287

Wech, A. G., Creager, K. C., Houston, H., & Vidale, J. E. (2010). An earthquake-like magnitude-frequency distribution of slow slip in northern Cascadia. *Geophysical Research Letters*. https://doi.org/10.1029/2010GL044881

Wiemer, S., & Wyss, M. (2000). Minimum magnitude of completeness in earthquake catalogs: Examples from Alaska, the Western United States, and Japan. *Bulletin of the Seismological Society of America*. https://doi.org/10.1785/0119990114

Yabe, S., & Ide, S. (2014). Spatial distribution of seismic energy rate of tectonic tremors in subduction zones. *Journal of Geophysical Research: Solid Earth*. https://doi.org/10.1002/2014JB011383

Zhang, P., Salman, O. U., Zhang, J.-Y., Liu, G., Weiss, J., Truskinovsky, L., & Sun, J. (2017). Taming intermittent plasticity at small scales. *Acta Materialia, 128*, 351–364. https://doi.org/10.1016/j.actamat.2017.02.039

1

[JGR: Solid Earth]

Supporting Information for

Tectonic low-frequency earthquakes in Shikoku, Japan: source scaling, size distribution and observational limits

M. Supino[1], N. M. Shapiro[2,3], J.P. Vilotte[1], N. Poiata[1,4] and K. Obara[5]

[1]Université de Paris, Institut de physique du globe de Paris, CNRS (UMR7154), F-75005 Paris, France.

[2]Institut des Sciences de la Terre, Université Grenoble-Alpes, CNRS (UMR5275), F-38058 Grenoble, France.

[3]Schmidt Institute of Physics of the Earth, Russian Academy of Sciences, Moscow, Russia

[4]National Institute for Earth Physics, 12 Călugăreni, Măgurele, 077125 Ilfov, Romania.

[5]Earthquake Research Institute, University of Tokyo, Bunkyo, Tokyo 113-0032, Japan.

Contents of this file

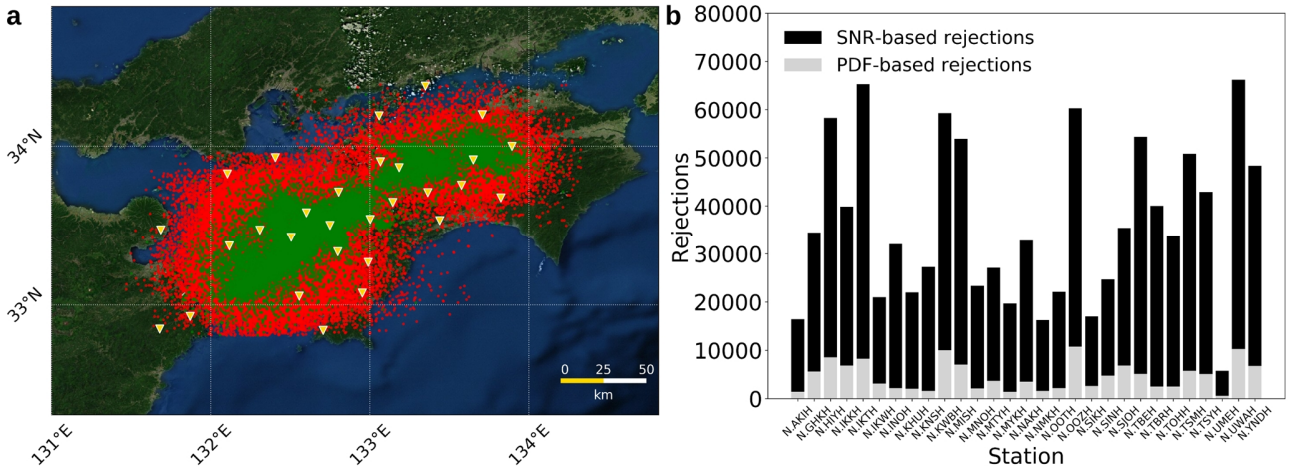

Figure S1. Automatic LFE catalog and events selection. a, Map view of the automatic LFE catalog. Events passing quality selection criteria are shown (green circles), together with rejected events (red circles). Yellow triangles indicate the Hi-net stations used for detection. **b,** Histogram of the number of rejections based on the signal-to-noise ratio criterion (black bars, see also Figure S4) or on the unconstrained marginal PDF criterion (grey bars, see also Figure S5-6).

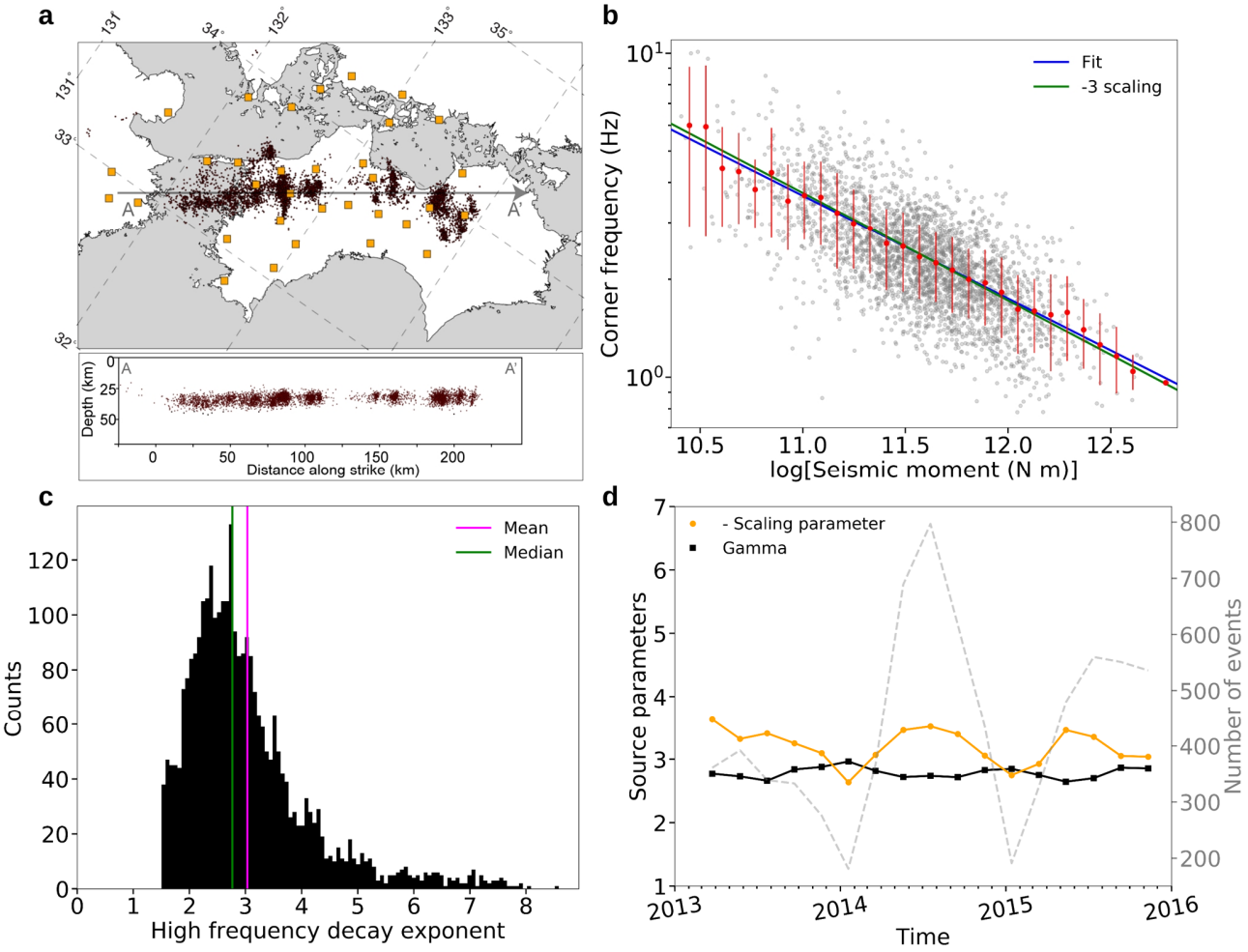

Figure S2. Source parameters of LFEs detected by JMA. a, Map view of the analyzed LFEs manually detected by JMA (black circles) and Hi-net stations used in this study (orange squares). The bottom panel show the depth cross-section of the events projected along strike direction A-A'. **b,** Estimated corner frequency and seismic moment of each LFE (grey circles), together with bin-averaged (bin-size = 0.08 log M_0) estimates (red circles) and related weighted standard deviations (red bars). The best fit line (blue line) has a scaling parameter *A'* = -3.2, according to eq. (2). The green line is the cubic scaling of regular earthquakes. **c,** Histogram of the estimated high frequency source spectra decay exponents. The green and magenta vertical bars are the median and mean of the distribution, respectively. **d,** Time variation of the scaling parameter (orange line) and of the high frequency decay exponent median value (black line). Parameters are evaluated in a 5-months moving time windows, with a time-shift of 2 months. The grey dotted line shows the number of events in each selected time windows.

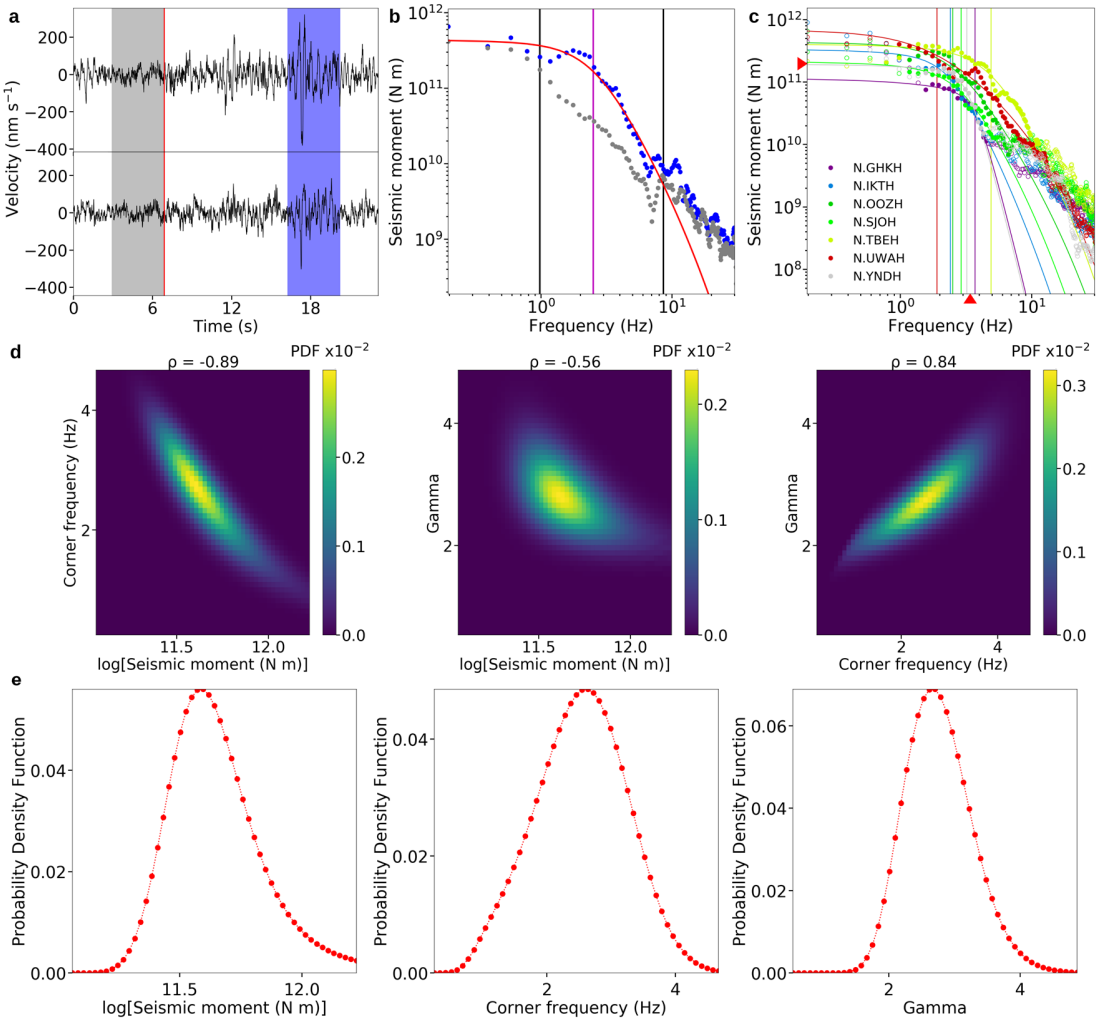

Figure S3. LFE source parameters estimation. a, LFE S-wave signal selected for the spectral inversion (blue box) and noise (grey box). The red vertical line shows the event origin time. Event-ID 20130604_1612I, Station N.OOZH. **b,** Displacement amplitude spectrum of the S-wave signal (blue circles) and of the noise (grey circles). The frequency band selected for the inversion, defined by the signal-to-noise ratio criterion (see section 3.1), is shown by the black vertical bars. The best-fit spectrum is the red curve. The magenta line shows the estimated corner frequency. **c,** Displacement amplitude spectra (circles) of all the stations inverted for the same event shown in panel (a). The continuous curves represent the best-fit spectra, the vertical lines show the corner frequency estimates. The red arrows show the final seismic moment and corner frequency estimated for the event. Colors are referred to the different stations (see key). **d,** 2-D marginal probability density functions of the source parameters log M_0, f_C and γ (high frequency source spectra decay exponent), and their correlation coefficients (top of the heatmap), obtained from the inversion of the spectrum in panel (b). **e,** Marginal probability density functions of the source parameters log M_0, f_C and γ (high frequency source spectra decay exponent).

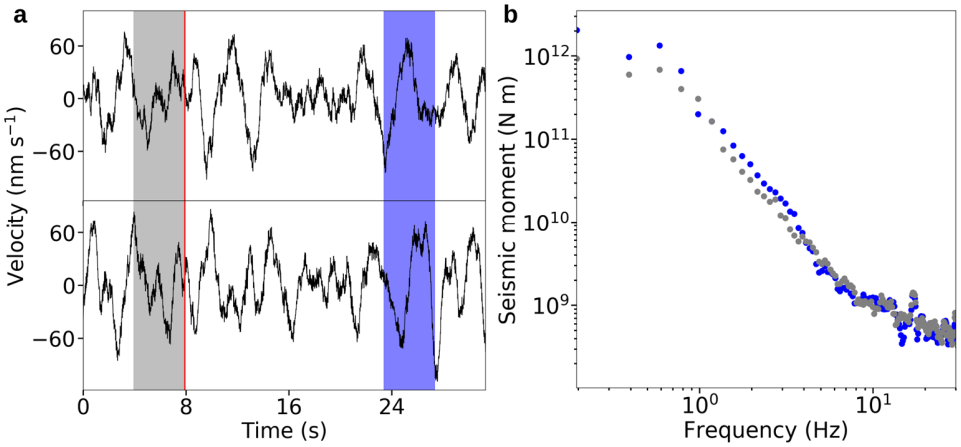

Figure S4. Rejected signal with noise-like spectrum. a, S-wave signal (blue box) and noise (grey box) of a rejected automatic detection. The estimated event origin time (red vertical line) is 2013/01/01, 18:23:37.45 (JST). Station N.GHKH. **b,** Displacement amplitude spectrum of the S-wave signal (blue circles) and of the noise (grey circles). The frequency band selected for the inversion is empty, as the spectral signal-to-noise ratio is lower than 1.25 in the whole frequency domain.

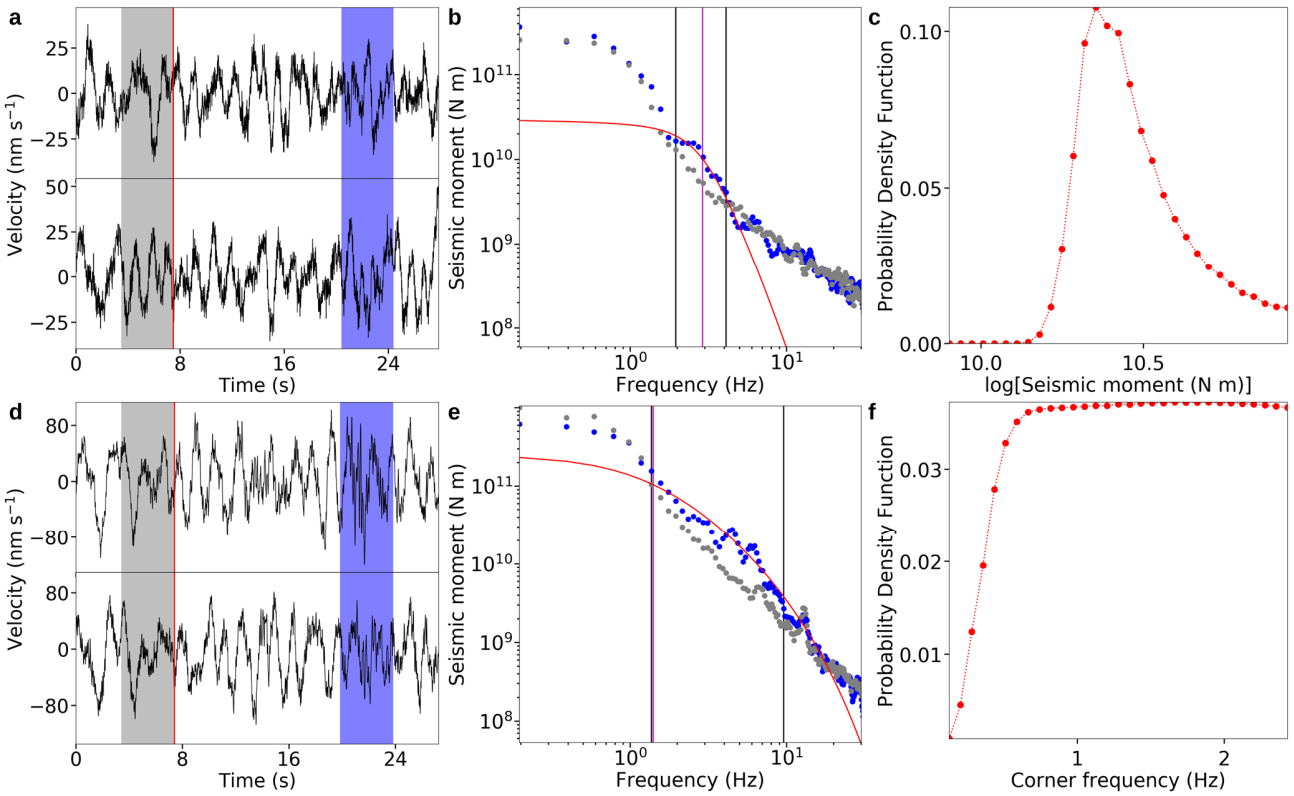

Figure S5. Rejected record with a very low signal-to-noise ratio. a, LFE S-wave signal selected for the spectral inversion (blue box) and noise (grey box). The red vertical line shows the event origin time. Event-ID 20130910_0014B, Station N.OOZH. **b,** Displacement amplitude spectrum of the S-wave signal (blue circles) and of the noise (grey circles). The frequency band selected for the inversion (black vertical bars), where the signal-to-noise ratio is larger than 1.25, is limited to 1.0 – 3.0 Hz . The best-fit spectrum is the red curve. The magenta line shows the estimated corner frequency **c,** The marginal probability density function of the source parameter log M_0 is unconstrained, because of the too limited information content of the noisy record. **d,** As for (**a**), Event-ID 20130604_1707B, Station N.INOH. **e,** As for (**b**), with frequency band = 1.5 – 10 Hz. **f,** As for (**c**), source parameter f_C (corner frequency).

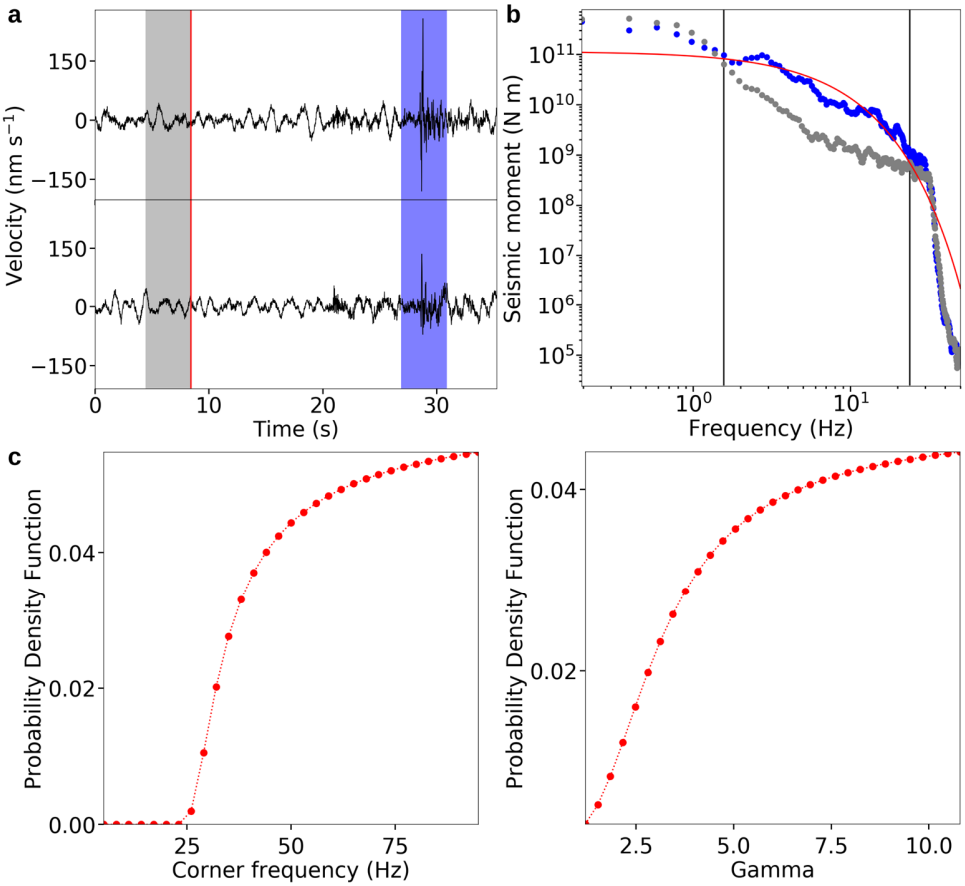

Figure S6. Rejected regular earthquake (false LFE detection). a, Regular earthquake signal wrongly detected as LFE by the automated detection method. The selected S-wave window (blue box) and noise window (grey box) are shown. The estimated event origin time (red vertical line) is 2015/08/03, 04:27:40.61 (JST). Station N.KNSH. **b,** Displacement amplitude spectrum of the S-wave signal (blue circles) and of the noise (grey circles). The best-fit spectrum is the red curve. The expected corner frequency (~ 60 Hz assuming a stress drop of 4 MPa) is well beyond the maximum frequency available for spectral inversion f_{MAX} ~ 30 Hz (right black vertical bar). The strong decay observed for frequencies larger than 30 Hz is due to the instrumental response function. **c,** The marginal probability density functions of the source parameters f_C (corner frequency) and γ (high frequency source spectrum decay exponent) are unconstrained, because the inverted observation (blue circles of panel **b**) is limited to a frequency band (black vertical bars of panel **b**) which does not carry information about the corner frequency or the source spectrum decay ($f_{MAX} \ll f_C$).

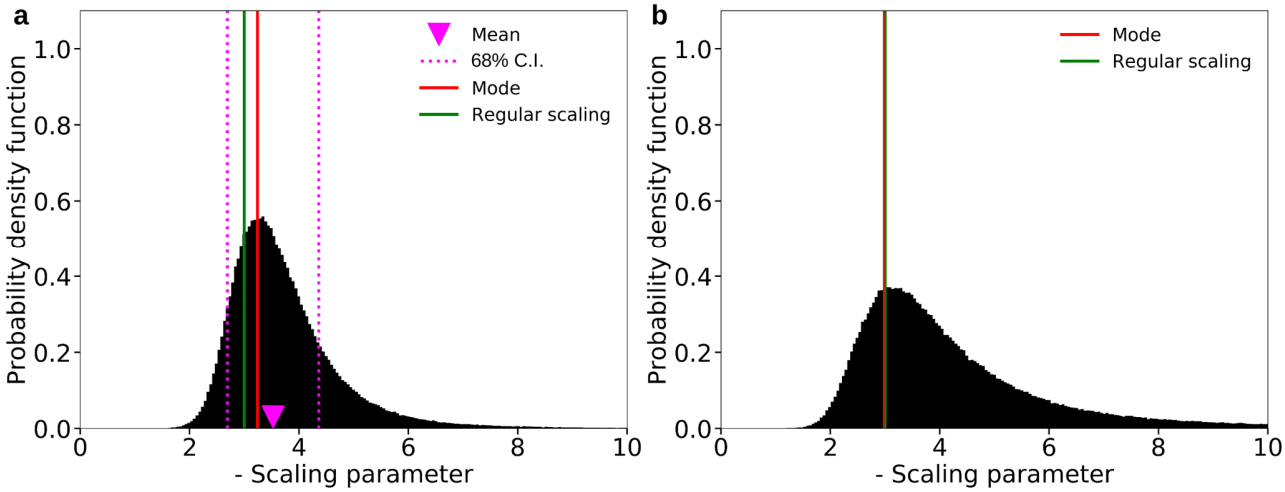

Figure S7. Probability density function of the scaling parameter. a, Probability density function (PDF) of the scaling parameter *A'* (see eq. (2)), estimated with a bootstrap method. Corner frequencies are randomly extracted 300,000 times for each bin represented in Figure 2 (log M_0 = 10.4 – 12.4), from gaussian distributions having mean and variance equal to the bin-averaged estimates. Magenta arrow and vertical dotted lines show mean and 68% confidence interval of the PDF, respectively. The red vertical line is the mode of the distribution, the green vertical line shows the scaling parameter of regular earthquakes (-3). **b,** As for (a), with log M_0 = 10.4 – 11.8. The seismic moment domain used for the PDF estimation excludes the bins that exhibit truncated corner frequency distributions (see Supplementary Fig. 9).

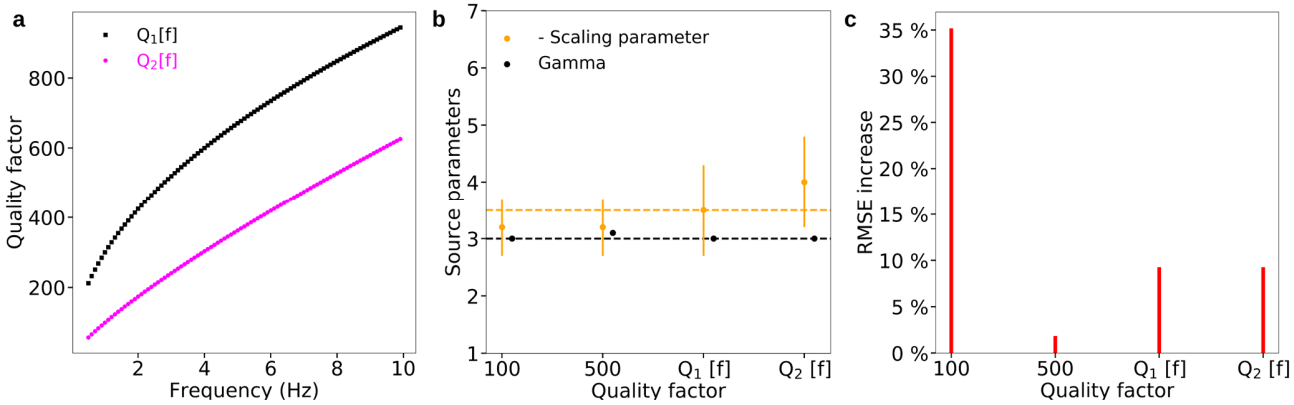

Figure S8. Anelastic attenuation effects on the estimates. a, Frequency-dependent quality factors used for the test inversions. $Q_1(f) = 300\ f^{0.5}$ (black curve), $Q_2(f) = 100\ f^{0.8}$ (magenta curve). **b,** Mean (orange circles) and standard deviation (orange bars) of the moment-duration scaling parameter PDFs, and median of the high-frequency source spectra decay exponent distributions (black circles), estimated for different quality factors. The values obtained for $Q = 300$ are shown by the dashed horizontal lines. **c,** Percentage increase of the RMSE mean value for different quality factors, with the case $Q = 300$ as reference value.

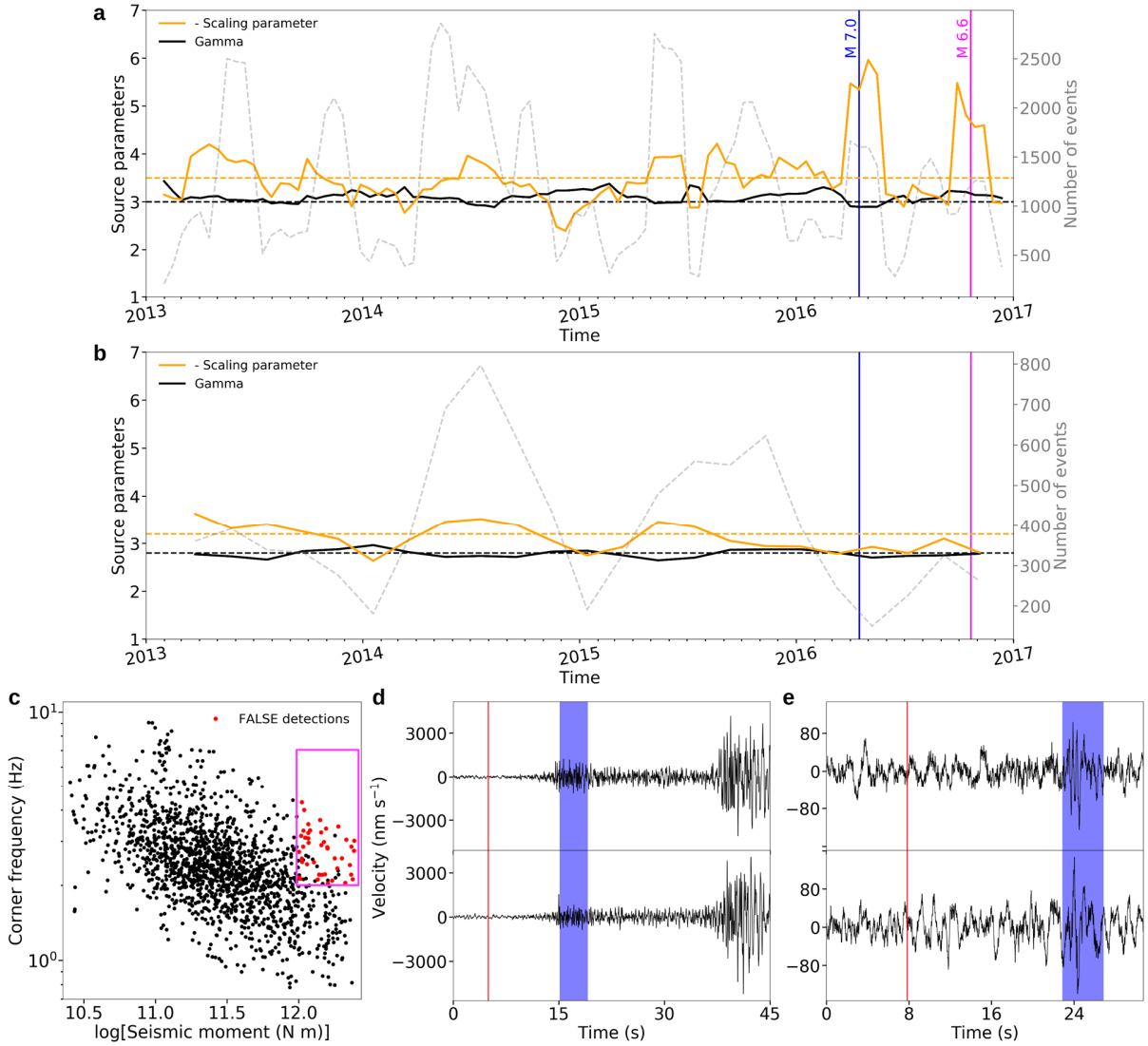

Figure S9. Aftershocks' contamination in the automatic LFE catalog. a, Time variation of source parameters represented as for Figure 3, with an extended time period including the year 2016. The origin times of the *M* 7.0 Kumamoto earthquake (blue vertical line) and of the *M* 6.6 Tottori earthquake (magenta vertical line) are shown. **b,** As for (a), for the JMA LFE catalog. **c,** Corner frequencies and seismic moments estimated from April, 1st 2016 to June, 1st 2016. The 58 events with log M_0 > 12.0 and f_C > 2.0 Hz (magenta box) have been visually inspected. Among them, 43 events were identified as false detections (red circles). **d,** Signal of a false detection. A portion of the P-wave of a ~200 km distant *M* 3.5 earthquake (JMA event-ID J2016041603520190) has been wrongly interpreted as the S-wave (blue box) of a ~40 km distant LFE. The origin time estimated for the false detection is shown by the red vertical line. Station N.HIYH, time relative to 2016/04/16, 03:52:21.5 (JST) **e,** Typical signal of a true detection, for a LFE with log M_0 = 12.0. The S-wave (blue box) is shown, together with the origin time.

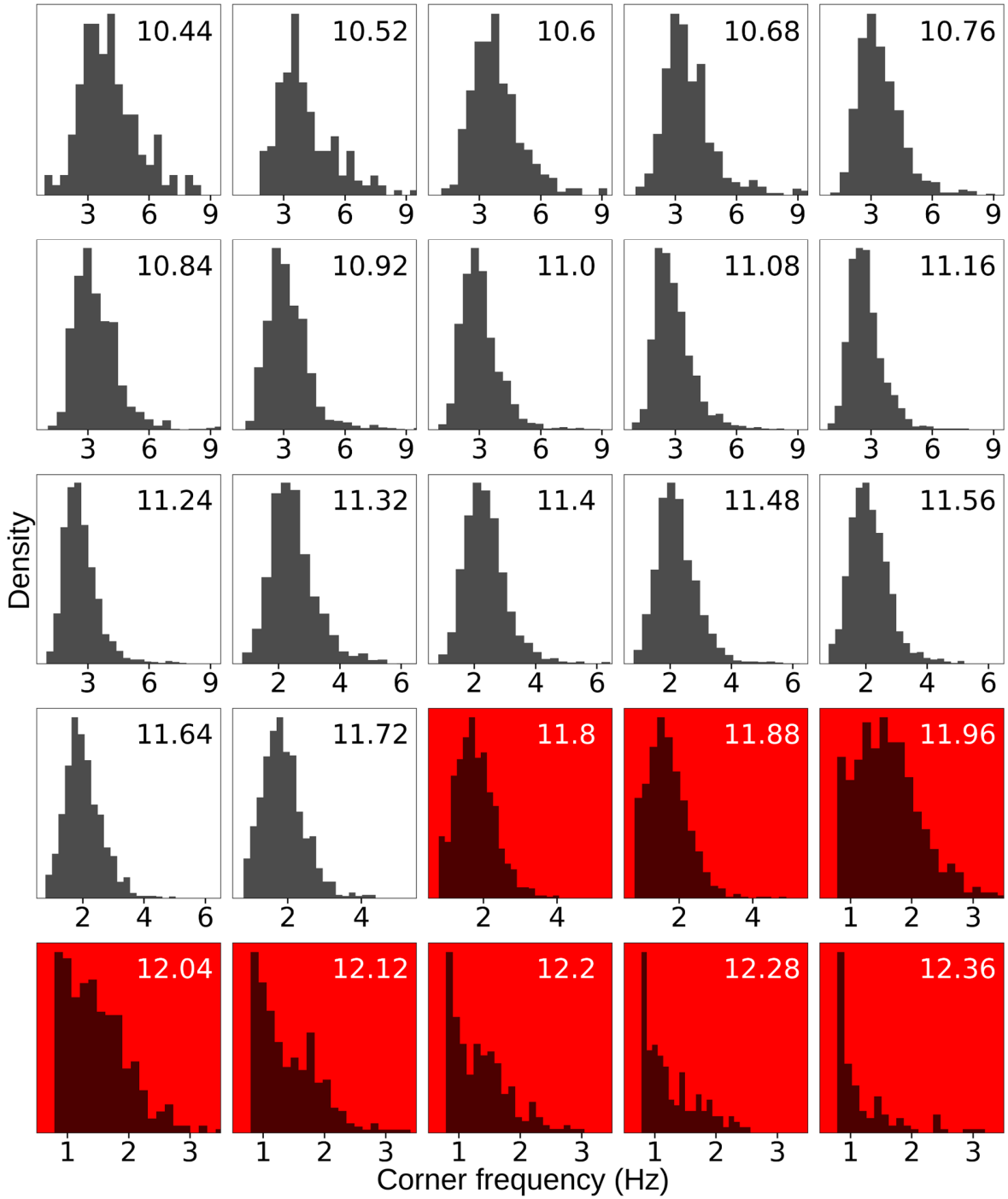

Figure S10. Corner frequency distributions for each bin represented in Figures 2a and 6. The central log M_0 value of the bin is shown in the upper right corner of the panels. The distributions are normal-like up to log M_0 = 11.72; red panels show bins with log M_0 ≥ 11.8, for which the left-truncated distributions suggest missing samples at low frequencies.

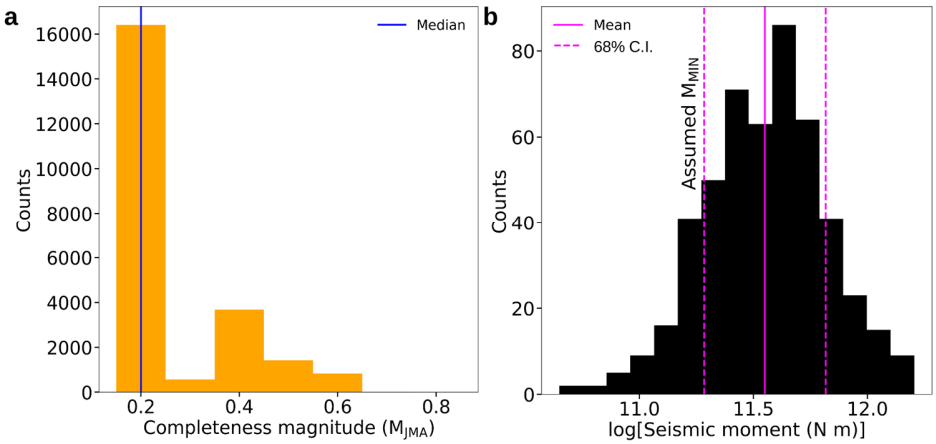

Figure S11. Estimation of completeness seismic moment M_{MIN}. a, Histogram of the completeness magnitudes (JMA-magnitudes) associated to each LFE of our automatic catalog from the earthquake detection probabilities estimated by Schorlemmer et al. (2018). The blue vertical line shows the median of the distribution. **b,** Histogram of the seismic moments estimated for all the events in the analyzed JMA catalog having a JMA-magnitude equal to the median of the distribution in panel (a), M_{JMA} = 0.2. The mean (magenta solid vertical line) and 68% confidence interval (magenta dashed vertical lines) are shown. We define as completeness seismic moment the lower bound of the 68% confidence interval.

Region	***B* (intercept)**	**Stress drop (kPa)**	**Number of events**	**Along-strike range (km)**
1	4.159 ± 0.005	29.3 ± 0.9	7957	0 – 75
2	4.153 ± 0.006	28.2 ± 1.1	4800	78 – 95
3	4.160 ± 0.007	29.5 ± 1.4	3648	97 – 121
4	4.129 ± 0.015	23.9 ± 2.4	643	127 – 145
5	4.125 ± 0.007	23.1 ± 1.2	2605	148 – 175
6	4.121 ± 0.009	22.6 ± 1.4	2259	179 - 213

Table S1. Scaling intercepts and related stress drop for along-strike regions of Figure 1 and Figure 4. Best fit intercept of the linear regression $\log f_C = A \log M_0 + B$, with A = -1/3 (fixed value), for the events occurring in each investigated along-strike region. The stress drop is evaluated using eq. (3), with k = 0.096 (V_R = 10% β) and β = 3700 m s^{-1}. The indicated along-strike ranges define the six regions.